

PVA-Based Nanofibers Containing Chitosan Modified with Graphene Oxide and Carbon Quantum Dot-Doped TiO<sub>2</sub> Enhance Wound Healing in a Rat Model

*Original*

PVA-Based Nanofibers Containing Chitosan Modified with Graphene Oxide and Carbon Quantum Dot-Doped TiO<sub>2</sub> Enhance Wound Healing in a Rat Model / Norouzi, F., Pourmadadi, M., Yazdian, F., Khoshmaram, K., Mohammadnejad, J., Sanati, M.H., Chogan, F., Rahdar, A., Bairo, F.. - In: JOURNAL OF FUNCTIONAL BIOMATERIALS. - ISSN 2079-4983. - ELETTRONICO. - 13:4(2022), p. 300. [10.3390/jfb13040300]

*Availability:*

This version is available at: 11583/2977772 since: 2023-04-05T14:31:55Z

*Publisher:*

MDPI

*Published*

DOI:10.3390/jfb13040300

*Terms of use:*

This article is made available under terms and conditions as specified in the corresponding bibliographic description in the repository

*Publisher copyright*

(Article begins on next page)

Article

# PVA-Based Nanofibers Containing Chitosan Modified with Graphene Oxide and Carbon Quantum Dot-Doped TiO<sub>2</sub> Enhance Wound Healing in a Rat Model

Fatemeh Norouzi <sup>1</sup>, Mehrab Pourmadadi <sup>2</sup> , Fatemeh Yazdian <sup>2,\*</sup> , Keyvan Khoshmaram <sup>2</sup>, Javad Mohammadnejad <sup>2</sup>, Mohammad Hossein Sanati <sup>1</sup>, Faraz Chogan <sup>2</sup> , Abbas Rahdar <sup>3,\*</sup>  and Francesco Baino <sup>4,\*</sup> 

<sup>1</sup> Department of Biology, Nourdanesh Institute of Higher Education, Meymeh, Isfahan 8351765851, Iran

<sup>2</sup> Department of Life Science Engineering, Faculty of New Science and Technologies, University of Tehran, Tehran 1439957131, Iran

<sup>3</sup> Department of Physics, Faculty of Science, University of Zabol, Zabol 538-98615, Iran

<sup>4</sup> Institute of Materials Physics and Engineering, Department of Applied Science and Technology, Politecnico di Torino, 10129 Torino, Italy

\* Correspondence: yazdian@ut.ac.ir (F.Y.); a.rahdar@uoz.ac.ir (A.R.); francesco.baino@polito.it (F.B.)

**Abstract:** Electrospun nanofibrous constructs based on nanoparticles and biopolymers have recently been used in tissue engineering because of their similarity to the extracellular matrix in nature. In this study, electrospun chitosan-carbon quantum dot-titanium dioxide-graphene oxide (CS-CQD-TiO<sub>2</sub>-GO) nanofibrous mats were synthesized for use as wound dressings by the electrospinning method. To increase the biodegradation rate and water resistance, the fabricated nanofibrous mats were cross-linked. SEM images showed a uniform and coherent structure of CS-CQD-TiO<sub>2</sub>-GO nanocomposites and CS-CQD-TiO<sub>2</sub>-GO electrospun nanofibers mats. FTIR analysis, XRD pattern, SEM mapping, and EDS spectrum demonstrate the accuracy of the synthesis as well as the elemental and chemical structure of the nanofibrous mat. The water contact angle indicated that the nanofibrous mat had a hydrophilic property, which is essential for controlling wound exudates. The tensile strength and elongation tests showed that the nanofibrous mat has suitable mechanical properties for wound dressing, including significant flexibility and strength. Interestingly, antimicrobial testing illustrated that the fabricated nanofibrous mat had antibacterial activity against Gram-negative and Gram-positive bacteria. Appropriate cell viability and cytocompatibility of treated mouse fibroblast NIH3T3 cells with the nanofibrous mat were determined using an MTT assay. The animal study results confirmed the proper potential of the nanofibrous mat in wound dressing applications.

**Keywords:** chitosan; poly(vinyl alcohol); carbon quantum dot; titanium dioxide; graphene oxide; wound healing



**Citation:** Norouzi, F.; Pourmadadi, M.; Yazdian, F.; Khoshmaram, K.; Mohammadnejad, J.; Sanati, M.H.; Chogan, F.; Rahdar, A.; Baino, F. PVA-Based Nanofibers Containing Chitosan Modified with Graphene Oxide and Carbon Quantum Dot-Doped TiO<sub>2</sub> Enhance Wound Healing in a Rat Model. *J. Funct. Biomater.* **2022**, *13*, 300. <https://doi.org/10.3390/jfb13040300>

Academic Editor: Anderson de Oliveira Lobo

Received: 6 November 2022

Accepted: 13 December 2022

Published: 15 December 2022

**Publisher's Note:** MDPI stays neutral with regard to jurisdictional claims in published maps and institutional affiliations.



**Copyright:** © 2022 by the authors. Licensee MDPI, Basel, Switzerland. This article is an open access article distributed under the terms and conditions of the Creative Commons Attribution (CC BY) license (<https://creativecommons.org/licenses/by/4.0/>).

## 1. Introduction

Wound healing issues and subsequent economic and health aspects involve millions of people all around the world [1]. Complex interactions between various cell types, elements of the extracellular matrix, and soluble factors are required for effective wound healing [2]. Therefore, the use of novel dressings that actively aid in wound healing has been taken into consideration [3]. Recent studies indicate that the use of nanoparticles (NP) in dressings plays an effective role in producing active dressings to accelerate wound healing [4]. Among efficient nanoparticles, TiO<sub>2</sub> shows antibacterial activity against some Gram-positive and Gram-negative bacteria strains. Good proliferation of animal fibroblast cells exposed to compounds containing TiO<sub>2</sub> also indicates that it is non-toxic [5]. However, TiO<sub>2</sub> is a photo-catalyst nanoparticle and is activated under the influence of harmful UV irradiation and can only use up to 5% solar energy [6]. Additionally, the low quantum

efficiency is a result of the low rate of electron transfers to oxygen. Therefore, it has been suggested that doping TiO<sub>2</sub> with carbon-based NPs will improve its separation of electron-hole pairs and move its absorption to the visible portion of the spectrum [7,8]. Combining TiO<sub>2</sub> with metal elements of carbon quantum dots increases the efficiency of nanoparticles [9]. CQDs as carbon-based NPs have multiple functional groups, such as carbonyl, hydroxyl, carboxyl, and amino groups, which increase the range of emission wavelengths and excitation [10]. This allows the CQDs to react easily with TiO<sub>2</sub> and reduce the TiO<sub>2</sub> bandgap energy to be activated in the visible light spectrum. The remarkable properties of carbon such as excellent dispersion, biocompatibility, low toxicity, good cell permeability, and easy functionalization with biomolecules have made CQDs applicable in drug delivery systems and wound-dressing [10–12]. The small size of CQDs makes them an attractive nanocarrier for drug delivery applications, and they have revealed negligible toxicity in animal studies [13]. Interestingly, recent studies have proven that the TiO<sub>2</sub>-CQD compound not only has antibacterial properties but is also a qualified option as medicine for wound healing [14]. On the other hand, some studies have suggested that combining graphene oxide (GO) with TiO<sub>2</sub> increases the antibacterial power of TiO<sub>2</sub> under solar energy. GO is a two-dimensional carbon-based nanostructure that has received much attention due to its potential of eliciting antibacterial effects, enhancing angiogenesis, improving cell proliferation, and facilitating rapid wound healing [15]. Furthermore, GO owns unique chemical and physical properties with diverse functional groups, high biocompatibility, and proper stability, which make it a favorable material for biomedical applications [16]. It has been demonstrated that incorporation of nanomaterials such as GO and reduced GO (rGO) with polymeric biomaterials can improve cell proliferation and blood vessel formation. Reducing GO minimizes the amount of oxygen as it makes GO unstable [17]. A recent work reported the angiogenic property of appropriate concentrates of GO and rGO through in vitro and in vivo angiogenesis assays by controlling reactive oxygen species (ROS) formation [18]. ROS can function as a signaling molecule in numerous growth factor-mediated physiological processes, including cell proliferation and wound healing [19]. However, the inherent aggregation characteristic of GO could result in dispersion restrictions that are strongly dependent on their surface interaction. To modify the GO surface, grafting hydrophobic nanoparticles could increase the layer gap and modify the GO behavior to a loose state while preserving its properties [20]. TiO<sub>2</sub> is an acceptable option for GO dispersion decoration. Thus, we have used GO in polymeric nanocomposite to accelerate wound healing and enhance cell migration. TiO<sub>2</sub>-CQD-GO nanocomposites (NC) have the potential of being both antibacterial and non-toxic. However, the use of nanocomposites is much more effective in nanofibers mode since nanofibrous structures exhibit surprising features such as high surface area-to-volume ratio and great porosity [21]. The ability of nanofiber-based NC to mimic the diameter of elongated collagen fibrils in the natural extracellular matrix makes it an ideal scaffold for tissue regeneration. Nanofibrous scaffolds offer an alternative artificial extracellular matrix for cell adhesion and proliferation due to their microporosity, antibacterial activity, surface roughness, hydrophilicity, and high surface area [22,23]. For instance, PVA nanofibers were fabricated in order to facilitate wound healing by incorporating carbon nanotubes and Ag nanoparticles [24]. PVA/ZnO nanocomposite fibers were also utilized for wound healing, which resulted in accelerated reepithelization, increased angiogenesis, and better cell attachment [25].

This study used chitosan (CS) polymer as a substrate for TiO<sub>2</sub>-CQD-GO NPs to facilitate nanofiber fabrication. Chitosan is a biodegradable and biocompatible polymer that can imitate the structure and function of the natural extracellular matrix. It is one of the many options used to produce biomedical nanofibers [26,27]. The electrospinning technique was used as one of the best methods for the production of polymeric nanofibers [21]. Since CS is hardly electrospinnable, it needs to be blended with an electrospinnable polymer such as poly(vinyl alcohol) (PVA) [28]. The reason for the preference of PVA over other polymers (e.g., poly(ethylene oxide)) is its desirable interactions at the molecular level with CS [21,29,30]. The novelty of this research was the synthesis of the CS-GO-CQD-TiO<sub>2</sub> NC,

which has been used after electrospinning as an effective antibacterial pad to accelerate wound healing.

## 2. Material and Methods

### 2.1. Chemicals and Materials

RPMI-1640, nitric acid (HNO<sub>3</sub>), phosphoric acid (H<sub>2</sub>PO<sub>4</sub>), sulfuric acid (H<sub>2</sub>SO<sub>4</sub>), phosphate buffer saline (PBS), graphite flakes, KMnO<sub>4</sub>, fetal bovine serum (FBS), MTT (3-(4,5-dimethylthiazol-2-yl)-2,5 diphenyl tetrazolium bromide), H<sub>2</sub>O<sub>2</sub>, and DMSO (dimethyl sulfoxide) were brought from Sigma (St. Louis, MO, USA). Diethylenetriamine, anhydrous tetrahydrofuran, thionyl chloride (SOCl<sub>2</sub>), poly(vinyl alcohol) (PVA), and dodecyl amine were bought from Merck, Germany, and the NIH 3T3 fibroblast cells were obtained from ATCC (Virginia, US).

### 2.2. Synthesis of Nanoparticles

#### 2.2.1. CQD Synthesis by Hydrothermal Method

Initially, 2 g of diammonium hydrogen citrate was added to 75 g of water and stirred until completely dissolved. After that, the mixture was put to the hydrothermal autoclave, which was then heated to 150 °C for 18 h. Finally, CQD was acquired at a concentration of 26.66 mg·mL<sup>-1</sup> [10,31,32].

#### 2.2.2. Synthesis of Graphene Oxide (GO)

There are various techniques for graphene production, including the Hummer method [15,33,34]. The initial step in the synthesis of GO monolayer is to add 1 g of graphite to 20 mL of 98% pure sulfuric acid on the stirrer within an ice bath to completely dissolve the graphite at a low temperature by a magnet within the sulfuric acid. After around 30 min, 3 g of potassium permanganate was progressively added to the solution, which had formed a green sludge. After roughly 30 min, 50 mL of distilled water was added dropwise. After 10 min, 100 mL of distilled water was added to the solution while swirling with a magnet. After 30 min, 35 mL of hydrogen peroxide was poured drop-by-drop, and the graphene oxide solution was removed from the heat stirrer after 24 h [35–38].

#### 2.2.3. Indirect CQD-TiO<sub>2</sub> Synthesis Method

An amount of 10 mL of CQD synthesized in the previous step was brought to a concentration of 2 mg·mL<sup>-1</sup>. In a separate vessel, 10 mg of TiO<sub>2</sub> was dissolved in 100 mL of distilled water. The two solutions were mixed for 1 h at 27 °C to homogenize thoroughly. Then, 0.2 g of sodium borate hydrate was poured into the solution as a reducing agent to react on the stirrer at room temperature for 2 h and release hydrogen gas. Finally, CQD-TiO<sub>2</sub> was gained at a concentration of 1.4 mg·mL<sup>-1</sup> [14].

#### 2.2.4. GO-CQD-TiO<sub>2</sub> Synthesis Method

In total, 100 mg GO was added to the synthesized CQD-TiO<sub>2</sub> to be completely homogeneous on the stirrer for 1 h. Then, 0.02 g of sodium borate hydrate was added and placed on a stirrer for 2 h to homogenize completely. Then, it was ultrasonicated for 10 min to dissolve the solution completely. Finally, a GO-CQD-TiO<sub>2</sub> nanocomposite was obtained at a concentration of 6.4 mg·mL<sup>-1</sup>. The freeze-drying method was also used to powder the sample. The sample was centrifuged and then refrigerated at -20 °C until it became completely frozen and finally dried.

#### 2.2.5. CS-GO-CQD-TiO<sub>2</sub> Synthesis Method

For the preparation of CS-GO-CQD-TiO<sub>2</sub> NC, the spraying method was used. For this purpose, 750 µL of CS-GO-CQD-TiO<sub>2</sub> NC solution was prepared with a concentration of 6.4 mg·mL<sup>-1</sup>. Then, pure glutaraldehyde (with a volume ratio of 0.05 glutaraldehyde/composite) in dark conditions was added to the solution to create cross-links and

increase the strength of the composite. Finally, the resulting solution was placed on a stirrer at room temperature for 5 min to obtain a homogeneous solution.

### 2.3. CS-GO-CQD-TiO<sub>2</sub> NC Electrospinning Process

In total, 0.5 g of PVA in 5 mL of DI water was dissolved on a stirrer under vigorous agitation for 1 h, and a homogeneous solution was obtained. The solution was then filled with 350  $\mu$ L of GO-CQD-TiO<sub>2</sub> NC solution and uniformly stirred for 30 min with a stirrer. With the use of a stirrer, 0.25 g of chitosan was dissolved in 0.6 mL of acetic acid and added to the pre-made nanocomposite solution and, finally, the solution was prepared for electrospinning. The NC solution was fed into a 5 mL syringe with a 22-gauge needle. Then, the syringe was placed in the appropriate position, as well as the attachment of two positive and negative electrodes to the aluminum foil of the collector plate to initiate the flow in the polymer solution. As a result, the electrospinning process began. Then, a syringe with a capacity of 5 mL was filled with the solution and located in the electrospinning setup. A constant flow of solution with a 0.5 mL·h<sup>-1</sup> rate, and constant conditions, including 15 kV voltage, 15 cm distance between the collector and tip of the needle, and 28 °C temperature, were applied. The electrospun sample was placed in the open air for 24 h to ensure the evaporation of any solvent.

### 2.4. Cross-Link Process of Nanofibers

The nanofibrous mats were cross-linked to enhance the mechanical characteristics. Additionally, cross-linking increases nanofiber water resistance ability. Cross-links originate from interactions between the polar hydroxyl groups of PVA, NPs, and chitosan's amine groups and the aldehyde groups of glutaraldehyde [39]. In this paper, glutaraldehyde was used to make cross-linking in the nanofibers. The sample was exposed to glutaraldehyde for 24 h in an oven desiccator at 50 °C. Because of the toxicity of glutaraldehyde, the nanofibers were washed with 1% glycine, and distilled water was used to remove unreacted glutaraldehyde. The samples were then placed in the oven to dry completely [40].

### 2.5. Morphological, Chemical, and Microstructural Characterization

Synthesized NPs and nanofibers were characterized by zeta potential, Dynamic Light Scattering (DLS), and Scanning Electron Microscope (SEM) techniques. The dry nanofibers were used in order to conduct SEM analysis. Furthermore, the nanocomposites were well dispersed in order to detect the size, zeta potential, and morphology through the mentioned techniques. Other characteristics were defined by Energy Dispersive X-ray Spectroscopy (EDS), SEM mapping, Fourier Transform Infrared Spectroscopy (FTIR), and X-ray Diffraction (XRD).

### 2.6. Static Water Contact Angles (WCA)

WCA was measured using the sessile-drop method. A specially sized drop (e.g., four microliters in ASTM D7334 standard) was applied to the sample [41]. The contact angle test was performed statically on the surface of the nanofibers using a Jikan Gac-10 device. A distilled water drop of approximately 4  $\mu$ L microliters was placed on the surface of nanofibrous mats measuring 2  $\times$  1 cm<sup>2</sup> at room temperature. A maximum of three drops was applied to each sample. Angles were then obtained using Image J: Drop-Analysis software and the mean of three measurements was reported for each sample. These angles indicate the wettability of the solid surface by the liquid [10,42].

### 2.7. Degradability of CS-GO-CQD-TiO<sub>2</sub>

To investigate the biodegradability of CS-GO-CQD-TiO<sub>2</sub>, the 1  $\times$  1 cm<sup>2</sup> fragment of the NC was dried, weighed, and placed in a Petri dish containing 10 mL of PBS with pH = 4.7 and stored at 37 °C for 30 min. Then, it was kept in the oven for 7, 14, 28, 42, 56, 72, and 96 h. Finally, the sample was incubated at room temperature for 3 days to dry completely,

and then its dry weight was measured using a digital scale. Degradability was obtained from the following formula [40]:

$$\text{Biodegradability (\%)} = \frac{\text{Primary dry weight} - \text{Secondary dry weight}}{\text{primary dry weight}} \times 100 \quad (1)$$

### 2.8. Antibacterial Properties of CS-GO-CQD-TiO<sub>2</sub> Nanofibers

The antibacterial activity of the nanocomposites was evaluated by using two indicator bacteria. The characteristics of the bacteria used are listed in Table 1.

**Table 1.** Characteristics of the bacteria used in antibacterial testing.

Bacterium Name	Standard Number	Gram Reaction
<i>Staphylococcus aureus</i>	PTCC1431	positive
<i>Escherichia coli</i> O157:H7	PTCC700728	negative

The liquid MIC of CS-GO-CQD-TiO<sub>2</sub> was obtained as reported in a previous article [14]. The sterile paper disk was coated with a minimal inhibitory concentration of CS-GO-CQD-TiO<sub>2</sub> at a rate of 100 g·mL<sup>-1</sup>. The disc was heated for 1 h at 45 °C to dry. *E. coli* and *S. aureus* were cultured uniformly with sterile swabs on Neutron Agar culture medium. Then, the CS-GO-CQD-TiO<sub>2</sub> disks were placed on the surface of each bacterium at a certain distance from the antibiotic disk. Furthermore, to test the growth inhibition zone made by CS-GO-CQD-TiO<sub>2</sub> NC, gentamicin for *S. aureus* and tetracycline for *E. coli* were employed as controls. Then, using a ruler to measure the growth inhibition zone’s diameter all around the discs, the data were evaluated using the standard CLSI table.

### 2.9. Cytotoxicity Induced by CS-GO-CQD-TiO<sub>2</sub> Nanofibers

CS-GO-CQD-TiO<sub>2</sub> NC was first extracted. Thus, for each 5 mg, the NC, 1 mL of culture medium was added. After incubation, the samples were added to mouse fibroblast cells at different concentrations of 0.01, 0.06, 0.1 µg·mL<sup>-1</sup>, and 0.6 at 3 and 5 day intervals. The culture medium was used as a control. In total, 10<sup>6</sup> NIH3T3 fibroblast mouse cells were cultured in a 96-well plate and then incubated for 24 h at 37 °C to evaluate cytotoxicity by the MTT method. Extracts from each sample were added to the respective wells on a plate, and the NIH3T3 cells were exposed to them for 24 h. Then, 100 µL of colorless PRMI and 10 µL of a 12 mM MTT solution were added to each well after the growth medium had been removed. The supernatant medium was removed after 4 h, and 100 µL of DMSO was added to each well. Finally, the amount of OD was calculated at 570 nm. The cytotoxicity test of samples was repeated three times, and the OD was measured in triplicate.

### 2.10. Tensile Strength and Elongation Tests

The mechanical characteristics were evaluated by assessing elongation-at-break and tensile strength with a Texture Analyzer in accordance with the Standard Test Procedure for Tensile Properties (ASTM) standard method [43]. These tests are carried out under circumstances where strips of preconditioned CS-GO-CQD-TiO<sub>2</sub> composite that are 1.0 cm (W) × 5.0 cm (L) in size are fitted between the machine’s grips with an initial grip gap of 50 mm. The sample was pulled from one side until broken at a cross-head speed of 2.0 mm/min. To obtain the average values, each test trial contained 5 replicate measurements. The tensile and elongation tests were shown by MPa (%) and percentage, respectively [3].

### 2.11. Cell Migration Inhibition Study by Scratch Wound Assay

A scratch wound assay was used to evaluate the effect of CS-GO-CQD-TiO<sub>2</sub> on cell migration. This test was performed with minor modifications similar to the technique used by Malmir et al. [14]. First, NIH3T3 fibroblast mouse cells were seeded in 24-well plates, and then they were given the night to attach to the plate bottom. After 2 h of starvation in 0.1% FBS medium, a sterile 10 µL pipette tip was used to puncture vertical

wounds at the cell surface. Cells were treated with CS-GO-CQD-TiO<sub>2</sub> and then incubated for 24 h at 37 °C. There was a 100 µm solution in each well. As a negative control, cells that were treated with the medium were used. At the beginning of the incubations and again after 24 h, the damaged cells were imaged using a Nikon Eclipse Te-2000-U microscope (4X magnification). Using Image J software, the scratch area's surface A was measured. For each well, the results were calculated using the following formula:  $100 \times (A_{t24}/A_{t0})$ . A Student's t-test was used in the statistical analysis, which was done using the Sigma Plot software.

### 2.12. Animal Study

By injecting 10 mg kg<sup>-1</sup> (body weight) of ketamine and xylazine intraperitoneally while the rats were under anesthesia, the dorsal area of their bodies was shaved from the scapula to the ileum, leaving a shear wound that measured 20 mm × 20 mm. They were then split into 4 groups, non-treated rats, phenytoin-treated rats, PVA-treated rats, and CS-CQD-TiO<sub>2</sub>-GO electrospun fiber-treated rats. The first day following wound induction, treatment was begun; topically applied polymers were used, and the wounds were treated. On the seventh and fourteenth days, all groups' wounds were inspected and photographed. Finally, the affected region was cleaned, captured on camera, and estimated with ImageJ software (version 1.44 p). The following formula was used to calculate the wound healing rate [9]:

$$\text{Wound healing (\%)} = \frac{W_0 - W_1}{W_0} \times 100 \quad (2)$$

where  $W_0$  and  $W_1$  refers to wound area at initial and interval time points, respectively.

A one-way ANOVA test analyzed the data obtained from the wound area measurement.

### 2.13. Histological Analysis

An identically positioned skin sample was taken from each mouse at the end of the experiment. The tissue samples were embedded in paraffin, fixed in 4% formaldehyde, and cut into slices that were about 4 mm thick. Hematoxylin, eosin (H&E), and TRM were used to stain the sections (Trichrome staining). Their morphological modifications were then assessed.

### 2.14. Statistical Analysis

The experiments in this study were repeated at least three times for each analysis, and the related data were expressed as mean ± standard deviation. ANOVA tests were performed based on groups using GraphPad Prism software. A *p*-value less than 0.05 was considered statistically significant.

## 3. Results and Discussion

### 3.1. Particle Size and Zeta Potential of CQD-TiO<sub>2</sub>

Evaluation of DLS test results for pure CQD, TiO<sub>2</sub>, and CQD-TiO<sub>2</sub> nanoparticles in Figure 1a,b shows the presence of nanoparticles with an average size of 9.14, 21.54, and 68.7 nm, respectively. CQDs are quantum NPs that may have a diameter of less than 10 nm [44]. Adding other NPs to CQDs leads to an increase in dynamic light scattering [10]. Therefore, the 59 nm diameter of CQD-TiO<sub>2</sub> NPs might be a preliminary indication that TiO<sub>2</sub> NPs are linked to CQDs. Figure 1c,d shows the zeta potential of pure CQD, TiO<sub>2</sub>, and CQD-TiO<sub>2</sub>. Particles with a zeta potential greater than 30 mV or less than -30 mV are stable. The reported zeta potential of -60.5 mV for CQD-TiO<sub>2</sub> indicates its good stability [45].

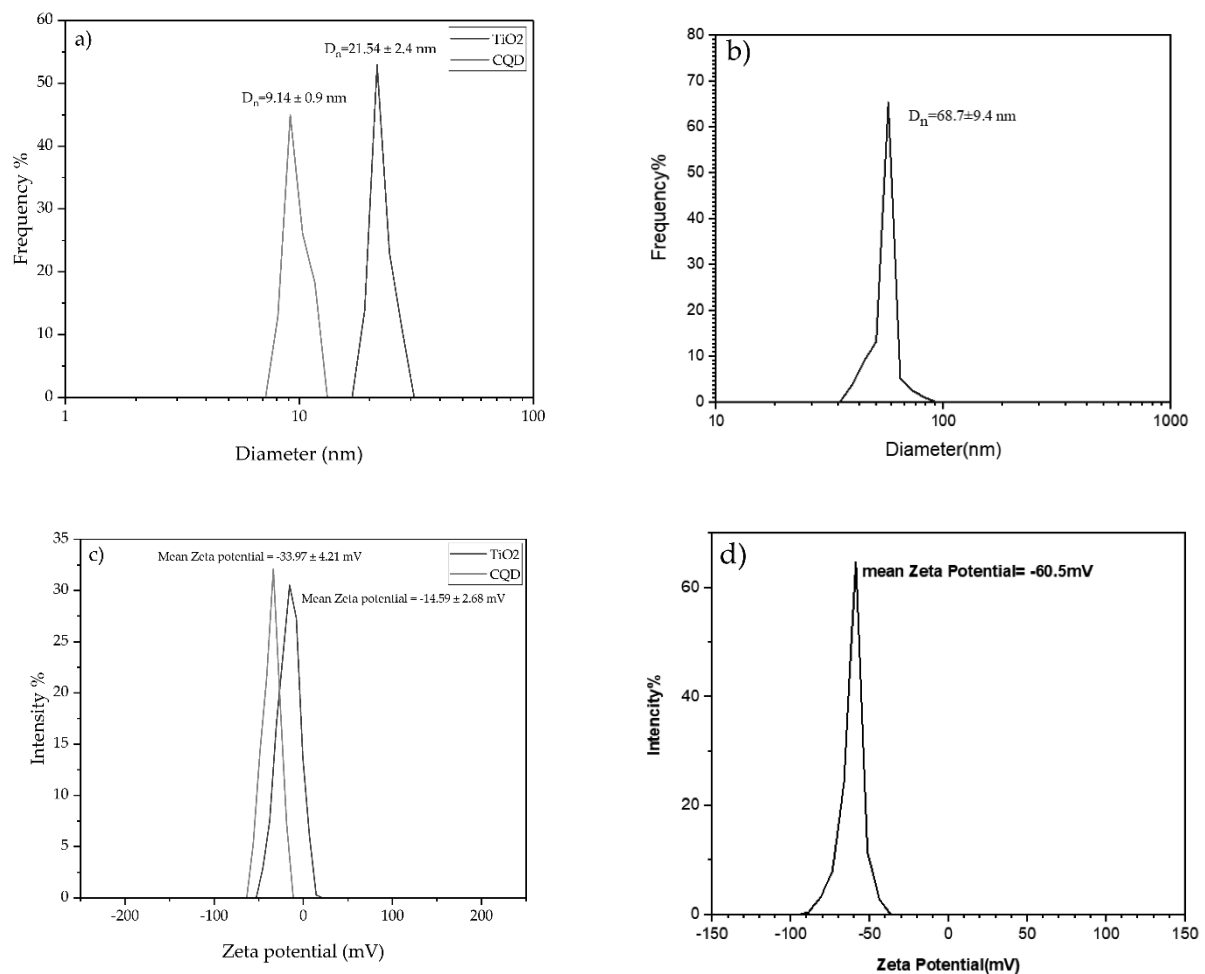


**Figure 1.** Dynamic light scattering of (a) CQD and TiO<sub>2</sub>, (b) CQD-TiO<sub>2</sub>; zeta potential of (c) CQD and TiO<sub>2</sub>, (d) CQD- TiO<sub>2</sub>.

### 3.2. Morphology of CS-GO-CQD-TiO<sub>2</sub>

The SEM images of the CS-GO-CQD-TiO<sub>2</sub>, electrospun PVA, and CS-GO-CQD-TiO<sub>2</sub> NC with a magnification of 10,000 times are displayed in Figure 2. In Figure 2 (top), a coherent structure with some roughness is seen. This compact structure indicates that the GO, CQD, CS, and TiO<sub>2</sub> NPs were well connected. The roughness seen in Figure 2 (top) is due to the presence of large chitosan crystals. The addition of CS to NC has minimized the free volumes and increased the cohesion of the microstructure of the NC [46]. The results of increased condensation and roughness due to the presence of chitosan in the NC is consistent with the results of Yaowen Liu et al. [47]. In this regard, the SEM images of the research of Ahmed et al. showed that the GO NPs are well dispersed in the synthesized polymer, and filling the porosity of the polymer is effective in its final performance [48]. Another study suggested that, according to SEM images, the presence of CS-GO NPs in the polymer increased the roughness and height of the polymer [49]. Figure 2 (bottom) shows the electrospun CS-GO-CQD-TiO<sub>2</sub> containing the PVA. The coherent surface and the obtained nanofibers illustrated the high compatibility of PVA with the NC and a compact structure lacking phase separation [50]. The absence of air bubbles, cracks, or pores further supports the excellent compatibility of the CS with PVA, as shown by Tripathi et al. [50].

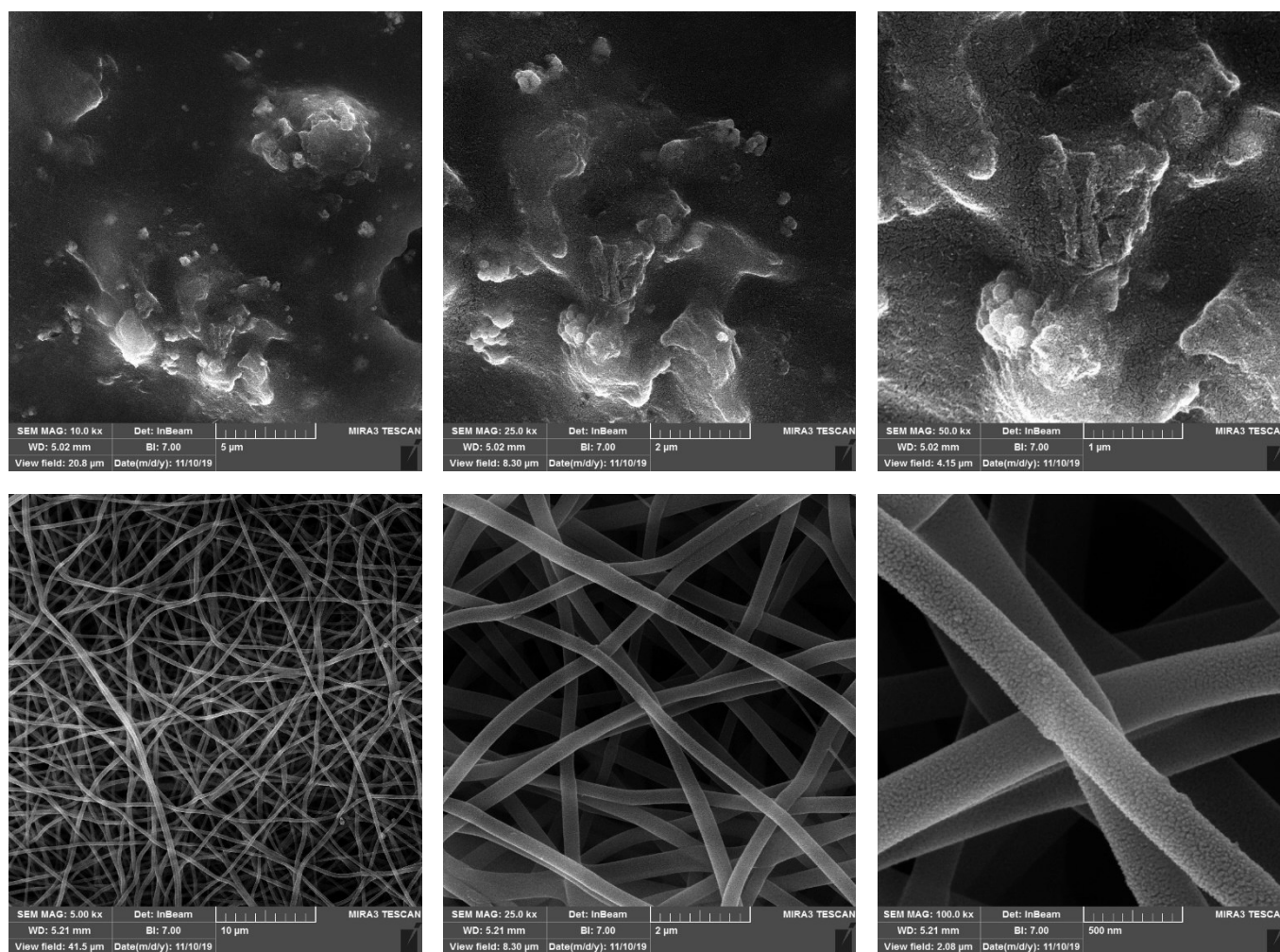


**Figure 2.** SEM morphology of (top) CS-CQD-TiO<sub>2</sub>-GO NC and (bottom) PVA and CS-CQD-TiO<sub>2</sub>-GO NC electrospun nanofibrous mat.

### 3.3. FTIR Analysis of Materials and Nanocomposites

FTIR analysis of GO, CQD-TiO<sub>2</sub>, and CS-GO-CQD-TiO<sub>2</sub> is illustrated in Figure 3a–c. Comparatively, in Figure 3a, GO plates have different peaks in the range of 1105 cm<sup>-1</sup> (C-O), 1200 cm<sup>-1</sup> (C-O-C), and 1600 cm<sup>-1</sup> (C=O), and are broadband in the range of 3000 to 3700 cm<sup>-1</sup>. Oxidizing agents have effectively oxidized the graphite as evidenced by the presence of oxygenated functional groups [51]. Furthermore, the detected bands of GO (Figure 3a) at 1628 and 1550 cm<sup>-1</sup> correspond to the carboxyl group bending vibration and the C=C skeletal vibration, respectively [52]. In Figure 3b, the C-OH tensile vibration peak is located between 1000 and 1300 cm<sup>-1</sup>, and the C-O-C bond exhibits vibration at 1163 cm<sup>-1</sup>. The absence of peaks in 1350–1460 cm<sup>-1</sup>, which is related to CQD, indicates that CQD-TiO<sub>2</sub> NPs are well-synthesized, and these results are similar to the recent papers [14]. The shifts of the peaks in Figure 3c indicate that the NPs in the CS-GO-CQD-TiO<sub>2</sub> are well-bonded together. According to relevant studies, chitosan has two firm peaks in 1534 cm<sup>-1</sup> and 1640 cm<sup>-1</sup>, which are related to amide II (N-H bending variations) and amide I (C=O stretching), respectively [53,54]. The C-O stretching in chitosan may be responsible for the absorption peak at 1090 cm<sup>-1</sup>. The C-H stretch vibrations are thought to be responsible for the peak at about 2900 cm<sup>-1</sup> [55].

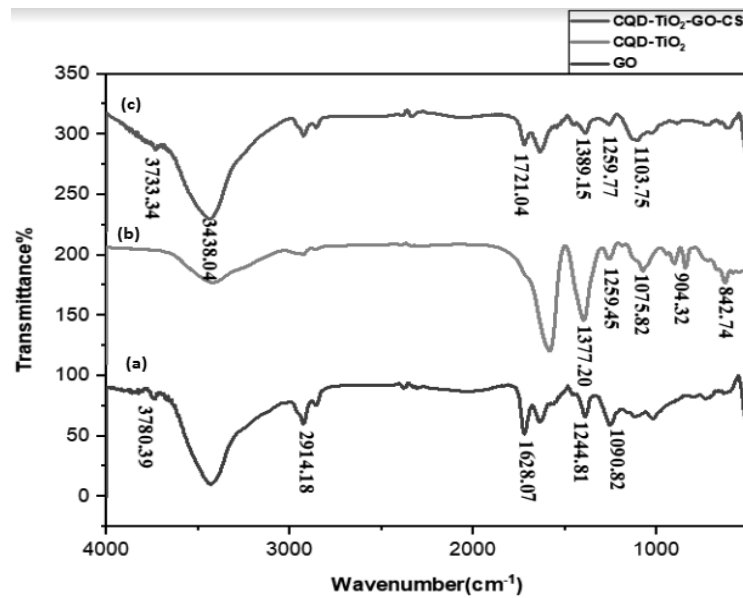


Figure 3. FTIR spectrum of GO (a), CQD-TiO<sub>2</sub> (b), CQD-TiO<sub>2</sub>-GO-CS (c).

### 3.4. FTIR Analysis of Nanofibers

Figure 4 reports the FTIR diagram of electrospun CQD-TiO<sub>2</sub>-GO-CS and PVA. To facilitate CS-GO-CQD-TiO<sub>2</sub> electrospinning, the NC has been combined with PVA [21]. Diana Isela and colleagues also combined chitosan with PVA in their research to facilitate the electrospun process of chitosan and nanofiber preparation [56]. Figure 4 indicates the FTIR of PVA. C-H tensile bond vibrations at 2916 cm<sup>-1</sup> and the C-O bond at 1372 cm<sup>-1</sup> belong to PVA. These results are in line with the results of Hassan Adeli et al. [40]. Characteristic absorption peaks of the components were shown by the nanofibrous PVA-CS-GO-CQD-TiO<sub>2</sub> mat. It is possible to attribute the O-H peak shift at the composite nanofibrous mat to the creation of hydrogen bonds between the hydroxyl or amino groups in CS and the hydroxyl groups in PVA in GO-CQD-TiO<sub>2</sub> and PVA in CS [57].

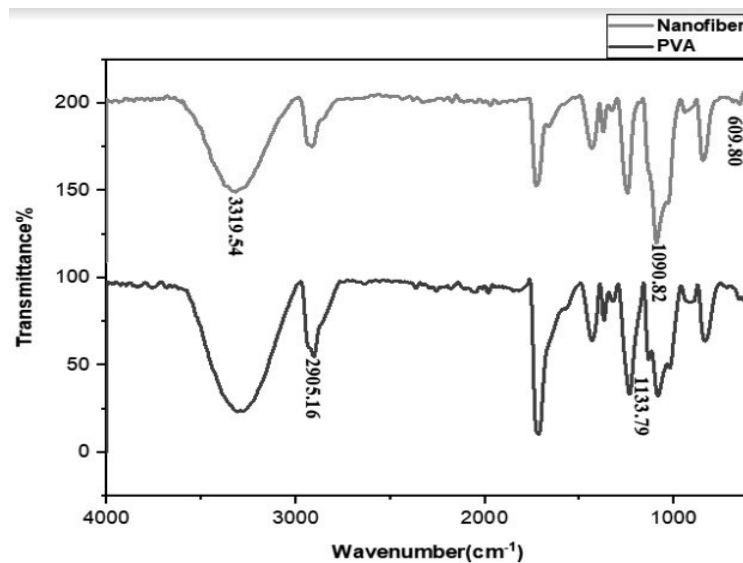
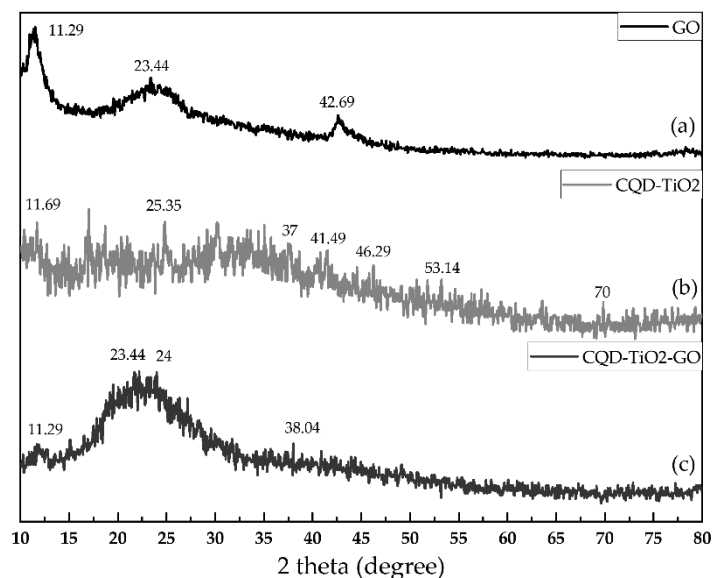


Figure 4. FTIR spectrum of PVA and CS-CQD-TiO<sub>2</sub>-GO electrospun nanofibrous mat. The red graph represents the CS-CQD-TiO<sub>2</sub>-GO nanofiber, and the black chart shows the PVA FTIR spectrum.

### 3.5. XRD Analysis

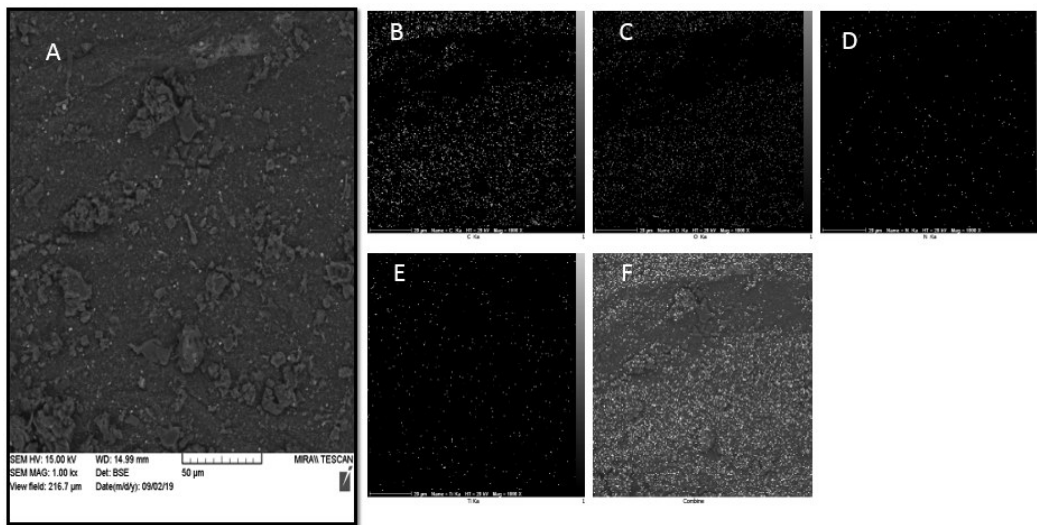
Figure 5a–c display the pattern of XRD from GO, CQD-TiO<sub>2</sub>, and CQD-TiO<sub>2</sub>-GO, respectively. According to previously published papers, graphene oxide has a peak in the  $2\theta \sim 10^\circ$  region with a base distance of  $d_{001} = 6.33 \text{ \AA}$ , which is used for characterization [58]. As shown in Figure 5a, the peak obtained from GO in the range of  $2\theta = 11.29^\circ$  and  $23.44^\circ$  is a characteristic of oxygen containing functional groups of GO. Another  $2\theta$  peak at  $42.69^\circ$  can be seen, which is attributed to the turbostratic band of disordered carbon components. These results are in accordance with Stengl et al. [59]. The XRD pattern of CQD-TiO<sub>2</sub> NPs in Figure 5b shows reflections at  $25.19^\circ$ ,  $37.77^\circ$ , and  $47.96^\circ$ , indicative of CQD-TiO<sub>2</sub>, and these results are consistent with our previous paper [14]. As illustrated in Figure 3c, the intensity of peaks was decreased, which can be caused by the amorphous behavior of synthesized nanocomposites and incorporation of CS; however, broad and weaker bonds of GO, TiO<sub>2</sub>, and CQD can be seen in the profile. The weak peak seen at  $2\theta \sim 10\text{--}12^\circ$  in Figure 5c indicates the presence of GO, which is caused by the small size of GO [59]. Studies have also shown that peaks around  $25.4^\circ$  are related to TiO<sub>2</sub> [60]. Therefore, it can be concluded that the peak created at  $2\theta = 24^\circ$  is the result of the overlap of CQD, TiO<sub>2</sub>, and GO NPs in the CQD-TiO<sub>2</sub>-GO NC.



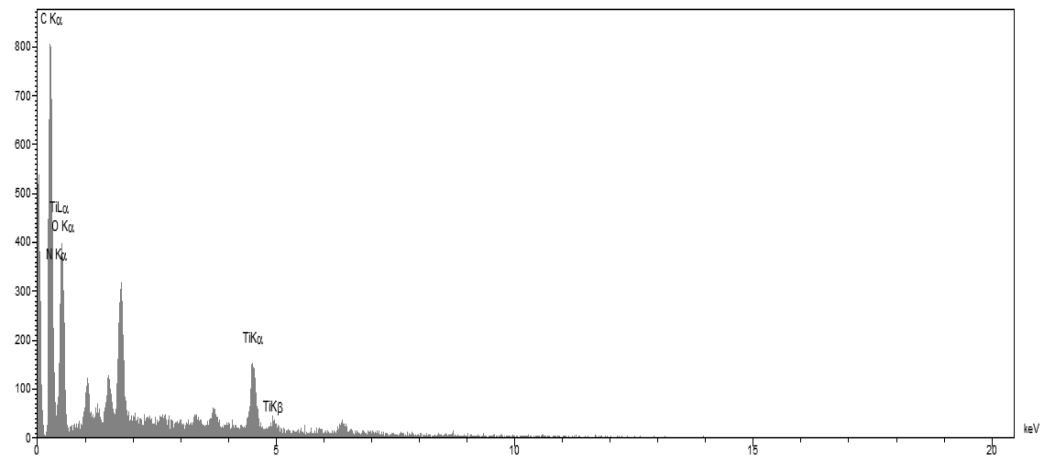
**Figure 5.** XRD pattern of GO (a), CQD-TiO<sub>2</sub> (b), GO-CQD-TiO<sub>2</sub> (c).

### 3.6. SEM Mapping and EDS Analysis

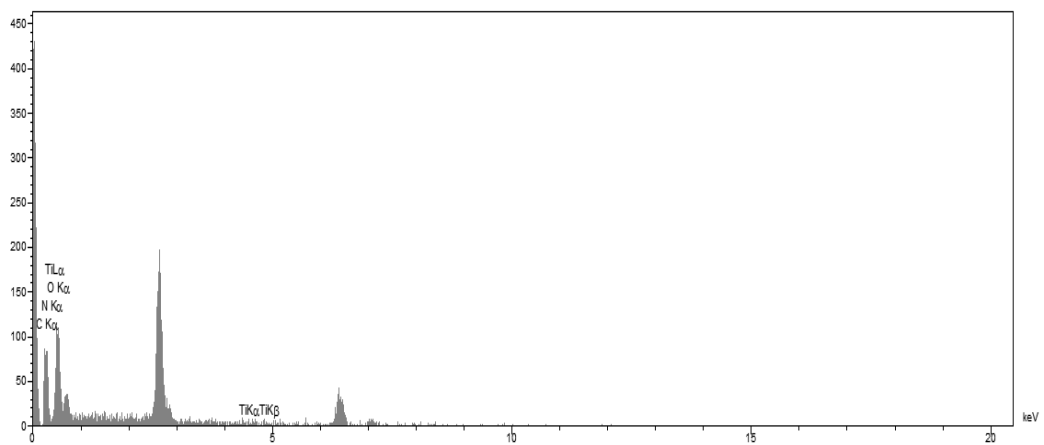
Figure 6a,b show SEM mapping and the EDS analysis of CS-CQD-TiO<sub>2</sub>-GO electrospun nanofibrous mats. SEM mapping for PVA was also carried out (Figure 6c) for the purpose of comparison. Figure 6a shows the uniform bead-free structure of the electrospun nanofibers. Similarly, Koosha et al. observed a uniform bead-free morphology for electrospun nanofibers of CS/PVA by SEM mapping and the EDS analysis [23]. The EDS spectrum of the electrospun nanofibers in Figure 6b confirmed the presence of C, O, N, and Ti elements related to CS, CQD, TiO<sub>2</sub>, and GO NPs. The presence of the Ti elements in comparison with Figure 6a,c indicates the significant distribution of the NPs in the PVA. Furthermore, the characteristic peaks of C, O, N, and Ti elements in Figure 6b were detected, showing that the NPs were uniformly distributed inside the nanofibers. The elemental compositions of the NC and nanofibers are reported in Table 2.



(a)



(b)



(c)

Figure 6. Cont.

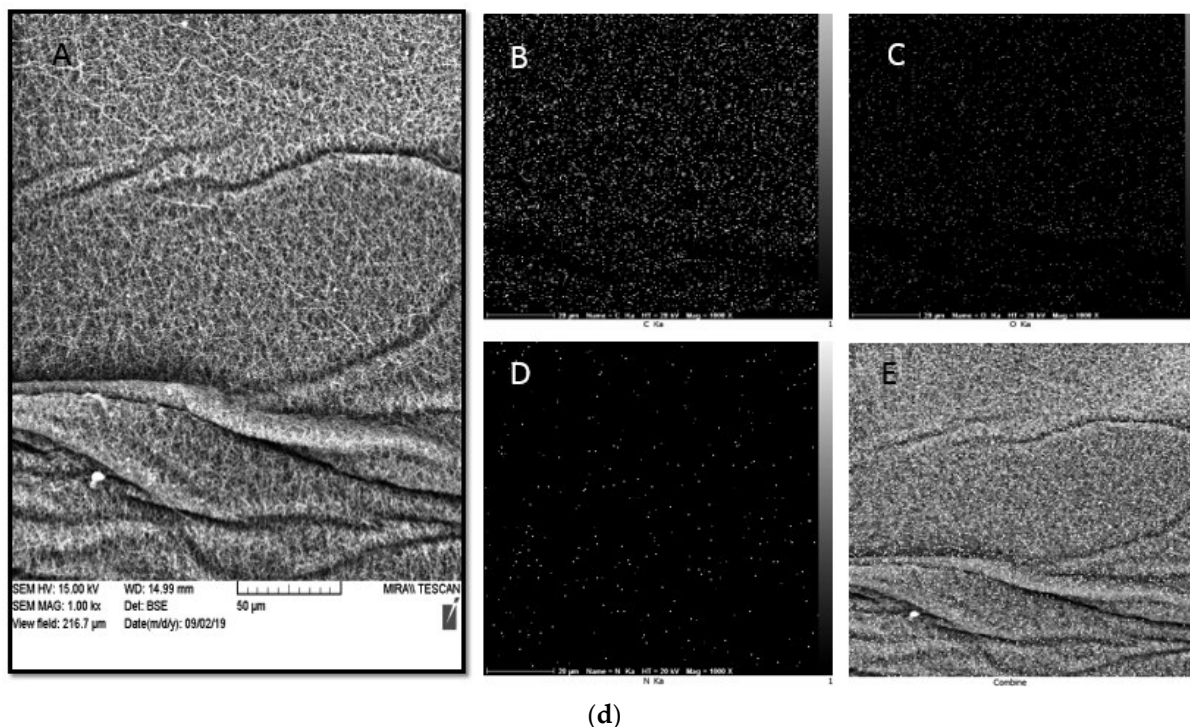


**Figure 6.** (a) Surface structure and elemental analysis of CS-GO-CQD-TiO<sub>2</sub> NC: (A) SEM morphology of CS-GO-CQD-TiO<sub>2</sub> NC; Images (B–E) represent carbon, oxygen, titanium, and nitrogen elements; Image (F) shows a combination of C, O, N and Ti elements. (b) EDS spectrum of CS-CQD-TiO<sub>2</sub>-GO NC. (c) EDS spectrum of CS-CQD-TiO<sub>2</sub>-GO electrospun nanofibrous mat. (d) Surface Structure and Elemental Analysis of PVA: (A) SEM morphology of PVA; Images (B–D) represent carbon, oxygen, and nitrogen elements; Image (E) shows a combination of C, O, and N elements.

**Table 2.** Elemental composition table of NC and CS-CQD-TiO<sub>2</sub>-GO electrospun nanofiber.

NC		CS-CQD-TiO <sub>2</sub> -GO Electrospun Nanofiber	
Element	wt.%	Element	wt.%
C	44.21	C	37.75
N	6.42	N	7.43
O	49.37	O	54.52
Ti	-	Ti	0.31

### 3.7. The Hydrophilicity of Different Electrospun Nanofibres

The secretions that are made during an ulcer to the surface of the wound create a favorable environment for the development of bacteria [61]. One of the critical variables in making a viable wound dressing is its capacity to assimilate water. The surface hydrophilicity of CS-CQD-TiO<sub>2</sub>-GO electrospun nanofibrous was evaluated using dynamic water contact angle (WCA) measurements. The WCA of CS-CQD-TiO<sub>2</sub>-GO electrospun nanofibrous mats is depicted in Figure 7. The nanofibrous mat’s WCA value was 66.65°. As mentioned in the articles, WCA over 90° means that the polymer surface is hydrophobic [62]. Therefore, it can be concluded that CS-CQD-TiO<sub>2</sub>-GO nanofibrous mats are hydrophilic. Notably, two essential factors affect the WCA value, namely the physical hydrophobicity of the material itself and the membrane surface roughness [63]. For example, in a previous paper, it has been shown that a hydrophobic polymer-based composite can be made by bonding hydrophobic substances to the surface of GO [64].



**Figure 7.** CS-CQD-TiO<sub>2</sub>-GO electrospun nanofibrous mat hydrophilicity. The angle  $\theta$  (WCA) is equal to 66.65°.

### 3.8. Weight Loss

The produced nanofibrous mats should have an adequate degradation rate to provide suitable dressing during the wound healing process [40]. Figure 8 shows the biodegradation rate of the mats immersed in the PBS solution. According to Figure 8, it is evident that in the early hours of the sample placement in PBS, the process of degradation of the composite with a steeper slope was performed. However, over time, the process has declined. Similar to these results, previous studies have shown that chitosan mats have a lower degradation rate than PVA, also revealing that chemical cross-linking between the amine groups of glutaraldehyde and chitosan causes slower depolymerization and less degradation [65,66].

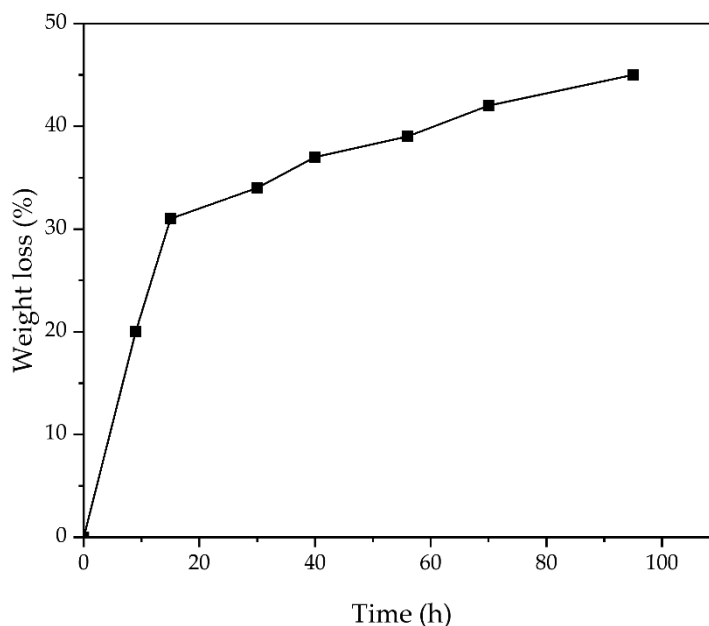


**Figure 8.** Weight loss of CS-CQD-TiO<sub>2</sub>-GO electrospun nanofiber. At first, biodegradability has increased, and it seems that this slope is almost fixed over time.

### 3.9. Mechanical Properties

The nanofibrous mats should be able to provide suitable mechanical characteristics and flexibility in the electrospun state for improved clinical operation in wound dressing application [67]. The resulting nanofibrous mats' elongation at break and tensile strength are shown in Figure 9b. The mechanical properties were suitable for the application in wound dressings and tissue engineering. The human skin elongation varies between 17% and 207% for elongation at break and between 1 and 32 MPa for tensile strength; however, because of the diversity of human skin, these values also rely on other variables such as age, genetic background, and skin color [68]. Figure 9b shows that the electrospun CS-CQD-TiO<sub>2</sub>-GO NC with PVA might offer greater tensile strength and elongation at break than the CS-CQD-TiO<sub>2</sub>-GO NC (Figure 9a). Notably, the synthesized mats in this research had very suitable mechanical properties, making the nanofiber flexible during wound coverage. Their tensile strength due to the presence of TiO<sub>2</sub> ceramic NPs is higher than that reported by Agrawal et al. for PVA/chitosan nanofibers (1.33–6.15 MPa) [65].

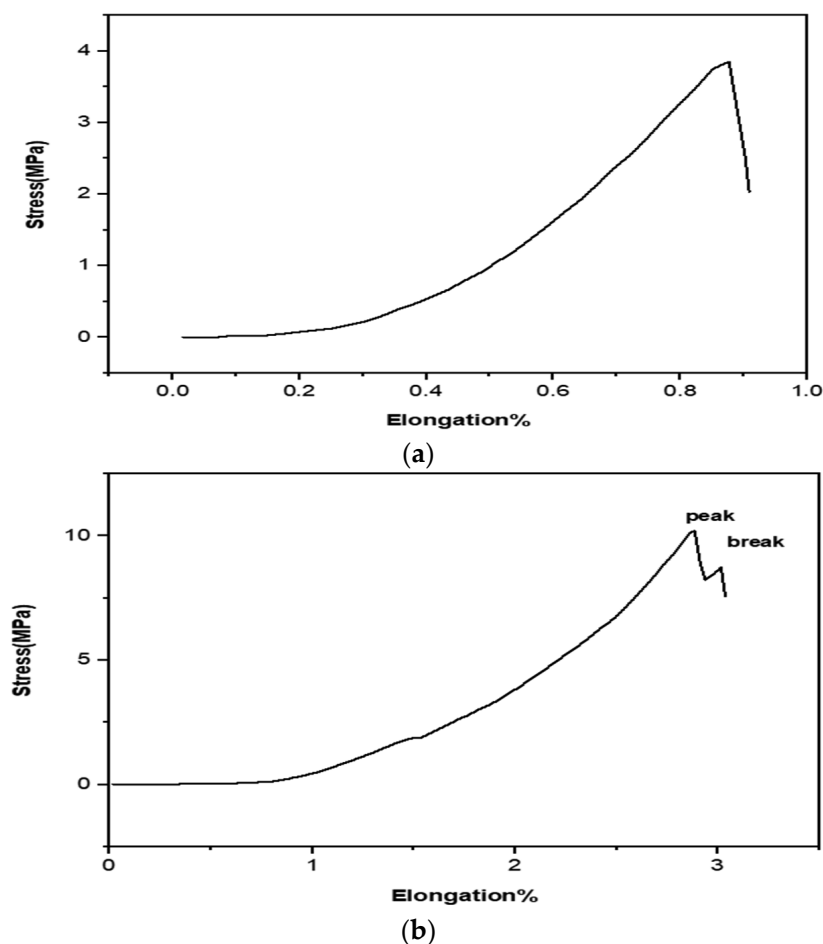


**Figure 9.** (a) Stress-elongation diagram in terms of pure bacterial cellulose. (b) Stress-elongation diagram in terms of bacterial cellulose/CS-CQDs-TiO<sub>2</sub>-GO electrospun nanofiber.

### 3.10. Cell Viability

It was anticipated that the perfect wound dressing must be significantly biocompatible [69]. An MTT assay was used to detect the cytotoxicity effects of the CS-CQD-TiO<sub>2</sub>-GO electrospun nanofibrous on Matson mouse fibroblast NIH3T3 cells. Figure 10 displays the results of this experiment at 0.06, 0.01, 0.6, and 0.1  $\mu\text{g}\cdot\text{mL}^{-1}$  concentrations based on nanocomposites compared to the control after 24 h. The NC solution was toxic at concentrations of 0.6 and 0.1  $\mu\text{g}\cdot\text{mL}^{-1}$ , which after one day caused growth inhibition in fibroblast cells. The NC at the concentration of 0.06  $\mu\text{g}\cdot\text{mL}^{-1}$  had almost no toxic effects (cell viability about 90%) on fibroblast NIH3T3 cells.

However, after 24 h, the concentration of  $0.1 \text{ g}\cdot\text{mL}^{-1}$  promoted the development and proliferation of fibroblast cells, proving the safety of the produced NC at this concentration rather than having toxic effects on the cells. The results demonstrated that CS-CQD-TiO<sub>2</sub>-GO nanofibrous mats are biocompatible and suitable for tissue engineering applications. The results are consistent with the studies of Hassan Adeli et al. on electrospun PVA-CS nanofibers [40].

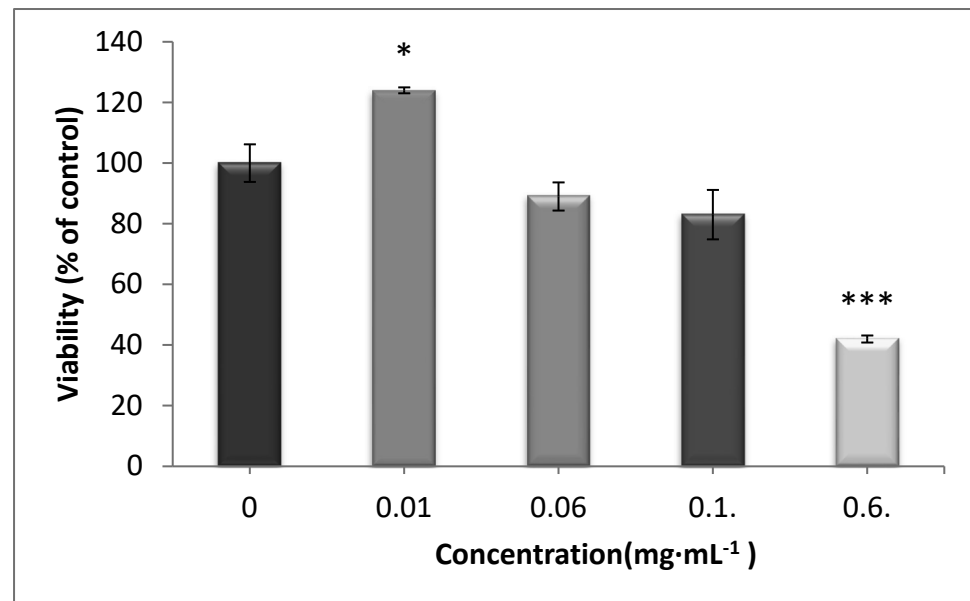


**Figure 10.** The cytotoxic effects of CQD-TiO<sub>2</sub>-GO-Cs NC on survival and proliferation of NIH3T3 fibroblast cells. The lowest toxicity was observed at the concentration of  $0.01 \mu\text{g}\cdot\text{mL}^{-1}$  (significant difference in comparison to control group: \*  $p < 0.05$  \*), and the highest toxicity was at the concentration of  $0.6 \mu\text{g}\cdot\text{mL}^{-1}$  of the NC (significant difference in comparison to control group: \*\*\*  $p < 0.001$ ).

### 3.11. Antibacterial Test

Previous studies have shown that *Staphylococcus aureus* bacteria are the main cause of wound infections [70]. Moreover, *Escherichia coli* bacteria are the common cause of burn wound infection [71]. Therefore, these bacteria can reduce the wound healing process [72]. The MIC concentrations of CQD-TiO<sub>2</sub>-GO-Cs NC were  $0.2 \text{ mg}\cdot\text{mL}^{-1}$  for *Staphylococcus aureus* and  $0.1 \text{ mg}\cdot\text{mL}^{-1}$  for *Escherichia coli*. The paper disc was impregnated with the NC at the above concentrations. Gentamicin and tetracycline discs were used as controls. The results in Figure 11A showed that the average halo diameter around the NC disk for *S. aureus* was 12 mm, and the halo diameter around the tetracycline antibiotic disk was 21 mm on average. As shown in Figure 11C, the inhibition zone of *S. aureus* around the sample and gentamicin antibiotic disk was approximately equal. In addition, the mean halo diameter around the NC disk in Figure 11B was 27 mm for *E. coli*, whereas the mean halo diameter around the tetracycline antibiotic disk was 29 mm. The gentamicin antibiotic and the NC disk's inhibition zones created in Figure 11D were approximately equal. The antibacterial activity was more effective toward the Gram-negative *E. coli* than Gram-positive *S. aureus* bacteria, presumably because of their different cell wall structures [70].

### 3.12. Inhibition of Cell Migration and Invasion

A scratch wound assay was carried out to determine whether the treatment of CS-CQD-TiO<sub>2</sub>-GO influenced cell migration and invasion. For the controlled cells, considerable cell migration was seen after 24 h, as illustrated in Figure 12. However, after being treated with CS-CQD-TiO<sub>2</sub>-GO, injured NIH3T3 fibroblast mouse cell monolayers swiftly healed the gap over the course of 24 h, just like in the control group.

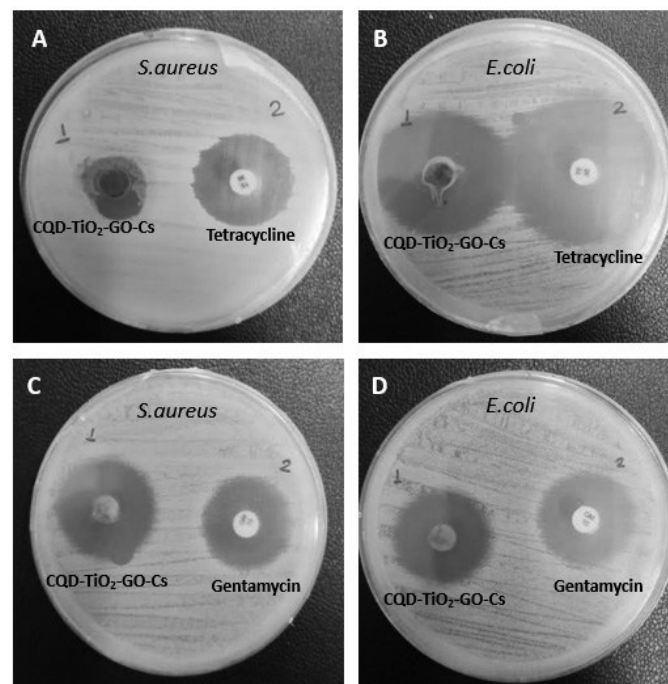


**Figure 11.** Comparison of antibacterial properties of CQD-TiO<sub>2</sub>-GO-Cs NC with tetracycline and gentamicin antibiotics. (A) *S. aureus*-containing plate with NC and tetracycline discs. (B) *E. coli*-containing plate with NC and tetracycline discs. (C) Plate containing *S. aureus* bacteria with NC and gentamicin discs. (D) plate containing *E. coli* with NC and gentamicin discs. Depending on the picture, the CQD-TiO<sub>2</sub>-GO-Cs NC has a more substantial effect on *E. coli* bacteria.

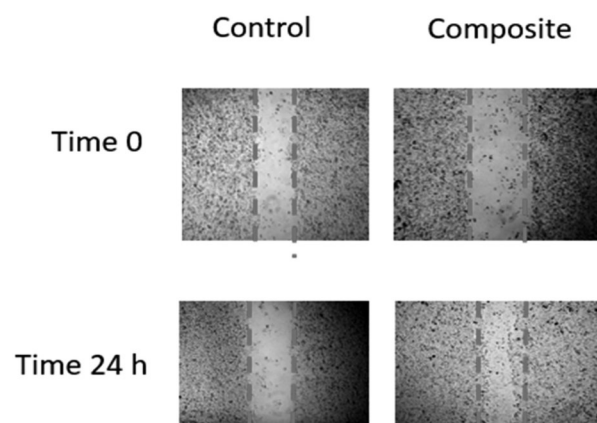


**Figure 12.** In vitro scratch test to measure the impact of the CQD-TiO<sub>2</sub>-GO-Cs NC on the migration of NIH3T3 fibroblast mouse cells. Then, at 0 and 24 h after scraping, cells were examined with an inverted microscope (4X magnification). The areas without cells are indicated by dotted lines.

### 3.13. Animal Study

Figures 13–15 display the percentage of improved wound healing over the course of the 14-day study in all animal groups that received treatment. On the fourteenth day after receiving CS-CQD-TiO<sub>2</sub>-GO treatment, the wound area was significantly reduced in mice. The CS-CQD-TiO<sub>2</sub>-GO electrospun nanofibrous mats group demonstrated the best wound healing effect on the 7th day with a 52.102% improvement in comparison to other groups. As shown in Figure 16, the wound healing of the phenytoin group was compared with other groups at both 7th and 14th day. The wound area of phenytoin was comparable with the positive and negative groups and did not show any significant difference, which might be due to normal wound healing function [73]. On the 14th day, the CS-CQD-TiO<sub>2</sub>-GO

electrospun nanofibrous mats group showed a 93.13% wound healing effect compared with both positive and control groups and phenytoin ( $p < 0.0001$ ) (Table 3). Motealleh et al.'s research outcomes are similar to these results [74]. Furthermore, the nanofibrous mats showed good collagen organization on mice skin, and inflammatory responses were not observed. Graph of Figure 16 shows the wound healing contraction rate measured on the first, 7th, and 14th days. The results illustrate that the highest rate of wound healing was in the group treated with nanofibrous mats after 14 days. Similar to this study, in a paper by Marulasiddeshwara et al., it was demonstrated that CS-TiO<sub>2</sub>, CS, and curcumin NPs have synergistic effects, and TiO<sub>2</sub>-CS-curcumin NC results in the wound healing of treated mice after 14 days [75].

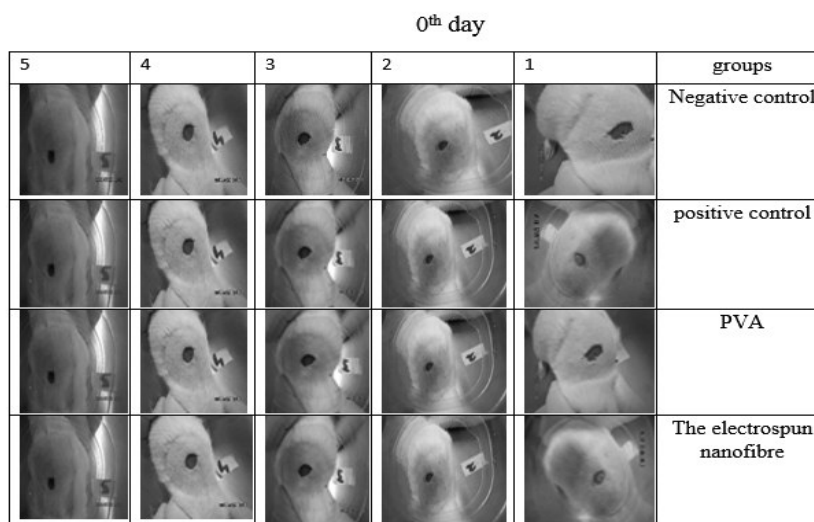


**Figure 13.** The rate of wound healing of 5 different mice treated in different groups on the first day. Wounds of about 1 cm × 1 cm were created in the skin of all mice, and mice were treated in different groups.

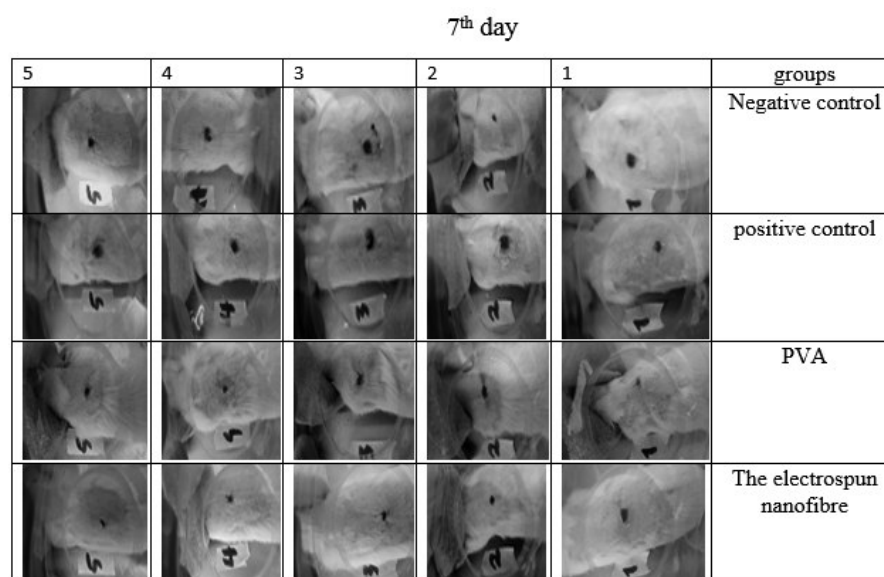


**Figure 14.** The rate of wound healing of 5 different mice treated in different groups on the 7th day. The highest rate of wound healing is related to the CS-CQD-TiO<sub>2</sub>-GO electrospun nanofiber treated group.

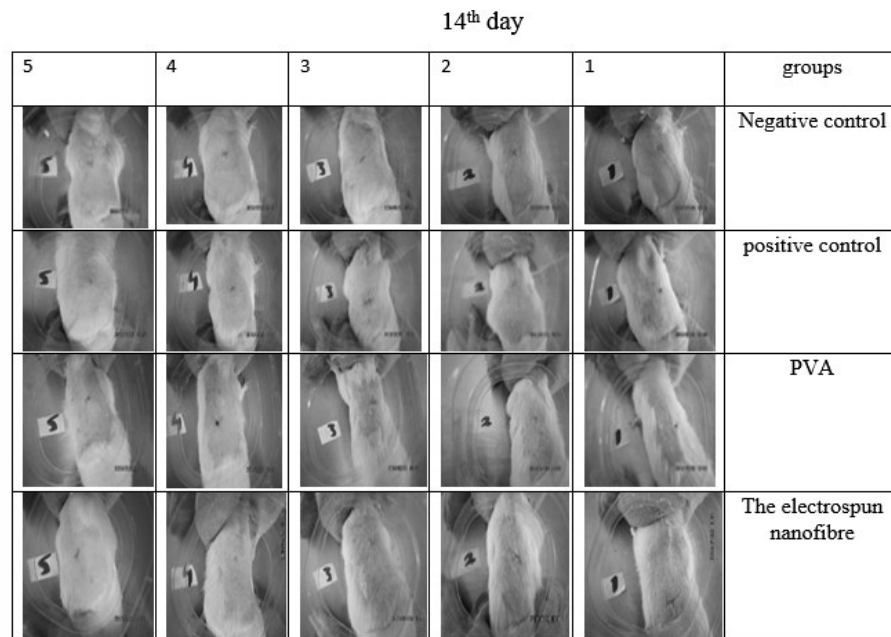


**Figure 15.** The rate of wound healing of 5 different mice treated in different groups on 14th day. As seen in the picture, the wounds of nanofibrous mat-treated mice have been completely healed.

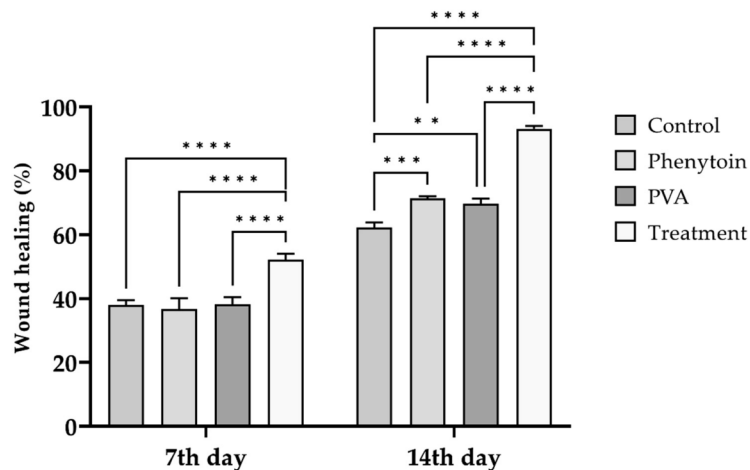


**Figure 16.** Graph of wound healing in the experimental groups after 7 and 14 days. According to the graph, the highest rate of wound healing was in the group treated with CS-CQD-TiO<sub>2</sub>-GO electrospun nanofibrous mats after 14 days. The treatment group had significant difference in comparison to other three groups at 14th day (\*\*\*\*  $p < 0.0001$ ); \*\* and \*\*\* reveal the difference between groups at  $p < 0.01$  and  $p < 0.001$ , respectively.

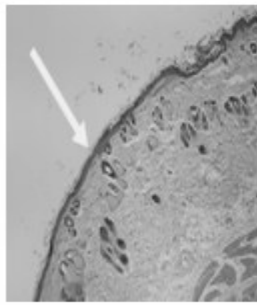
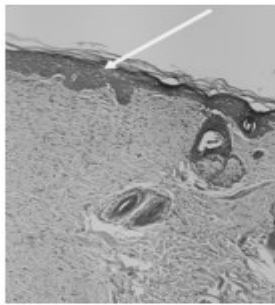
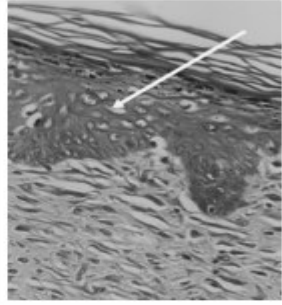
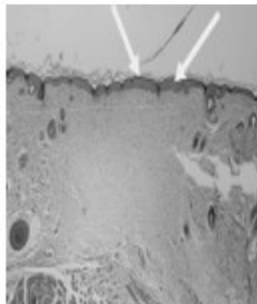
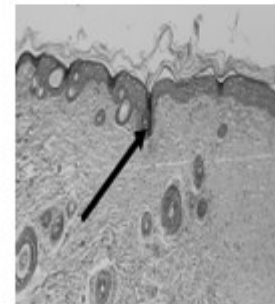
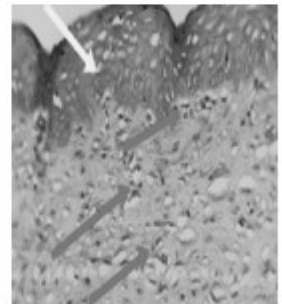
**Table 3.** Wound healing percentage in experimental groups.

Groups	7th Day	14th Day
Control	38.025 ± 1.484	62.175 ± 1.583
Phenytoin	36.675 ± 3.435	71.34 ± 0.669 <sup>a</sup>
PVA	38.163 ± 2.257	69.659 ± 1.597 <sup>a,e</sup>
CS-CQD-TiO <sub>2</sub> -GO nanofibrous mats	52.102 ± 1.861 <sup>c</sup>	93.137 ± 0.885 <sup>b,d</sup>

Values are presented as mean ± standard deviation, <sup>a</sup> significantly different from control,  $p < 0.01$ , <sup>b</sup> significantly different from control,  $p < 0.001$ , <sup>c</sup> significantly different from PVA,  $p < 0.05$ , <sup>d</sup> significantly different from Phenytoin,  $p < 0.001$ , <sup>e</sup> significantly different from CS-CQD-TiO<sub>2</sub>-GO electrospun nanofibrous mats,  $p < 0.001$ .

### 3.14. Histology

Different epidermis layers can be well identified in the histological images in Figures 17–20. To evaluate the effects of the CS-CQD-TiO<sub>2</sub>-GO nanofiber on the skin of injured mice, the wound skin tissue was examined in four groups after 14 days of treatment. The histology of all samples was examined by staining with H&E and TRM dyes. A similar method was performed by Bolle et al. [76] and Murphy et al. [77]. The negative control group included samples not receiving any treatment (Figure 17). The positive control group included the group treated with phenytoin (Figure 18). Figure 19 shows the group treated with the CS-CQD-TiO<sub>2</sub>-GO nanofiber and the last group treated with the CS-CQD-TiO<sub>2</sub>-GO nanofiber containing phenytoin (Figure 20). According to the results obtained from microscopic imaging of the four treatment groups and their comparison with each other, the wound healing stages in the CS-CQD-TiO<sub>2</sub>-GO nanofiber group containing phenytoin were more comprehensive than in the other three groups. This group also had an inflammatory response within 14 days after wound healing. It gradually decreased in this group, and dead cells in the tissue were much less seen than in the other groups, and creatine formation was observed on the fourteenth day.

Negative control group (no wound dressing)			
×40	×100	×400	Type of staining
			H & E
			TRM

**Figure 17.** Microscopic imaging of skin tissue sections stained by two types of H&E and TRM dyes. The photo shows improved skin tissue 14 days after treatment in the non-wound dressing group. Yellow arrows indicate the formation of an epidermal layer in the tissue repaired with phenytoin, and also the green arrows indicate the penetration of inflammatory cells into the repaired tissue. Black arrow indicates dead cells in the tissue.

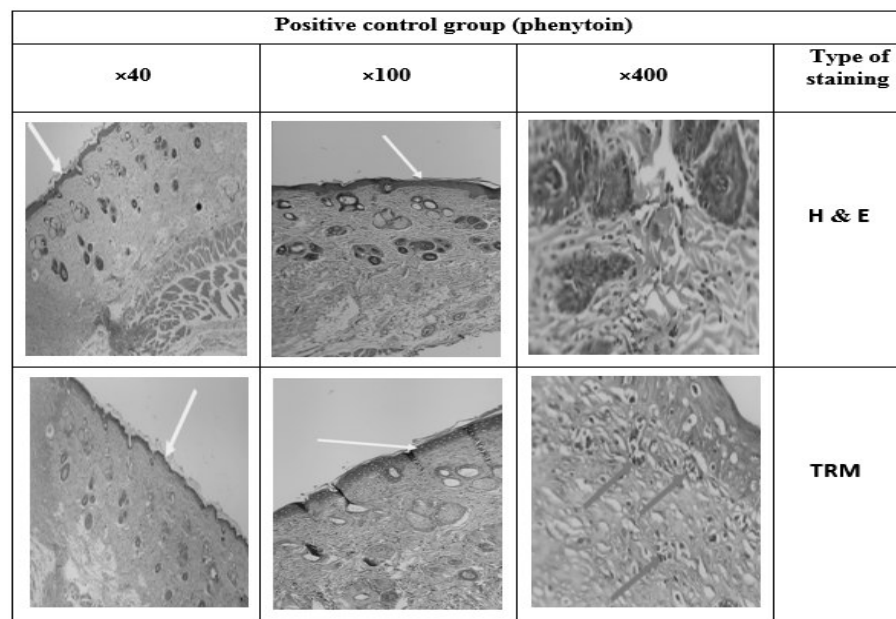


**Figure 18.** Microscopic imaging of improved tissue incisions 14 days after treatment in the positive control group (phenytoin). The yellow arrows indicate the formation of an epidermal layer in the repaired tissue that is treated with phenytoin, and the green arrows indicate the penetration of inflammatory cells into the repaired tissue.

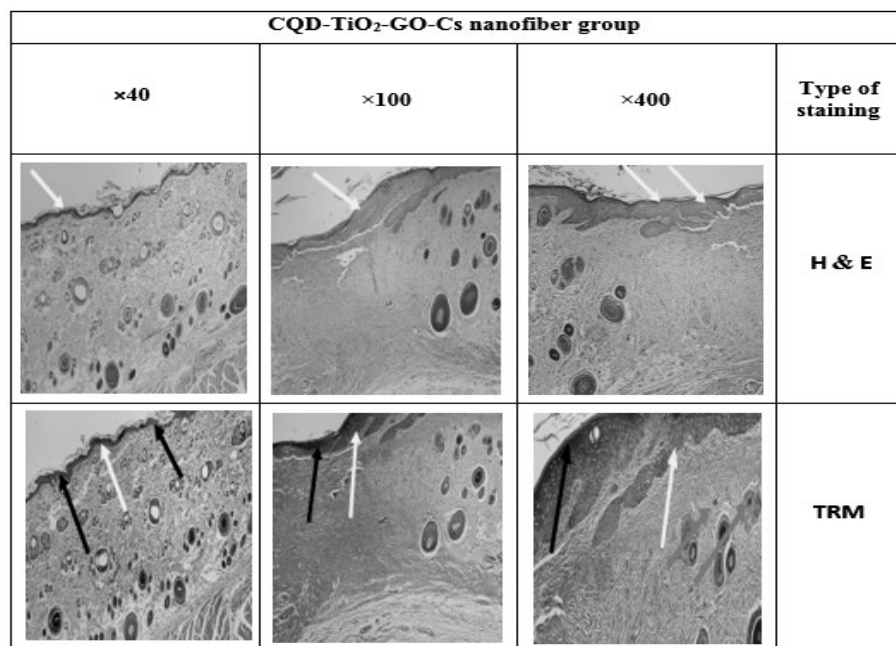


**Figure 19.** Microscopic imaging of improved tissue incisions 14 days after treatment with CQD-TiO<sub>2</sub>-GO-Cs nanofiber. Yellow arrows indicate the formation of an epidermal layer in the restored tissue treated with CQD-TiO<sub>2</sub>-GO-Cs nanofiber, and black arrows indicate dead cells in the tissue. Additionally, the green arrows indicate the penetration of inflammatory cells into the repaired tissue.

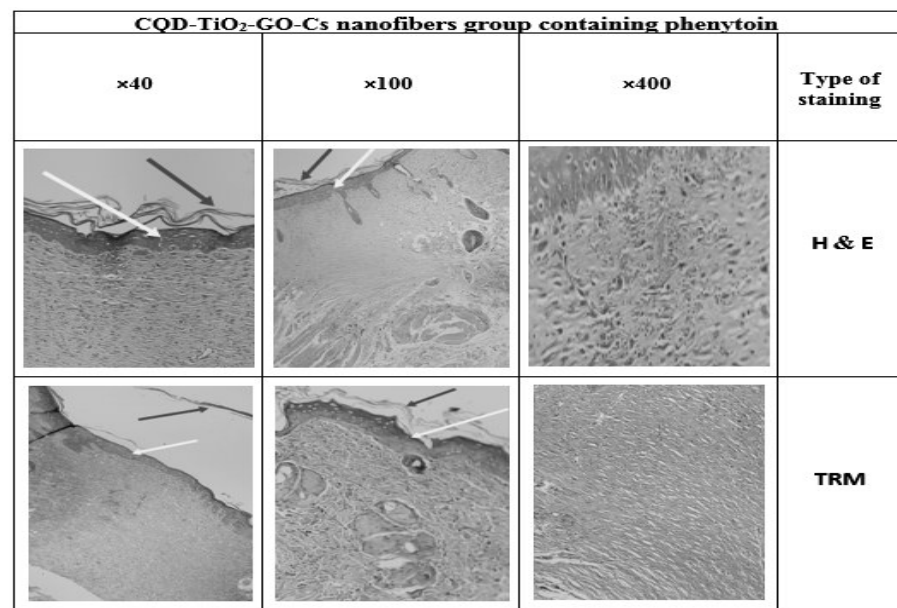


**Figure 20.** Microscopic imaging of improved tissue incisions 14 days after treatment with CQD-TiO<sub>2</sub>-GO-Cs nanofiber containing phenytoin. The yellow arrows indicate the formation of an epidermal layer in the repaired tissue along with the CQD-TiO<sub>2</sub>-GO-Cs nanofiber containing phenytoin. The purple arrows indicate the formation of creatine in the tissue.

#### 4. Conclusions

In this study, novel electrospun nanofibrous CS-CQD-TiO<sub>2</sub>-GO mats were fabricated for wound healing application. FTIR analysis, XRD pattern, and SEM morphology indicated proper incorporation of NPs into composite and bead-free and uniform structures of the electrospun nanofibrous mats. Furthermore, the EDS spectrum of nanofibers confirmed the presence of related elements to CS, CQD, TiO<sub>2</sub>, and GO. The size and zeta potential of CQD-TiO<sub>2</sub> were 68.7 nm and −60.5 mV, respectively. The mechanical properties were also investigated and the presence of the ceramic phases played a key role in increasing the tensile strength from around 3.8 to 9.0 MPa. Furthermore, the mats exhibited effective activities to inhibit bacterial growth of both Gram-positive and Gram-negative bacteria and showed proper cytocompatibility. The results of in vivo experiments in mice indicated that the CS-CQD-TiO<sub>2</sub>-GO composite resulted in better reepithelization and wound healing compared to the control group.

**Author Contributions:** Conceptualization, M.P.; Investigation, F.N., M.P., F.Y., K.K., J.M., M.H.S., F.C., A.R. and F.B.; writing—original draft preparation, F.N., M.P., K.K., J.M., M.H.S. and F.C.; writing—review and editing, A.R., F.Y. and F.B.; supervision, F.Y. All authors have read and agreed to the published version of the manuscript.

**Funding:** This research received no external funding.

**Data Availability Statement:** All data are included in the article.

**Conflicts of Interest:** The authors declare no conflict of interest. The authors declare that they have no known competing financial interests or personal relationships that could have appeared to influence the work reported in this paper.

#### References

1. Lamboni, L.; Li, Y.; Liu, J.; Yang, G. Silk sericin-functionalized bacterial cellulose as a potential wound-healing biomaterial. *Biomacromolecules* **2016**, *17*, 3076–3084. [CrossRef] [PubMed]
2. Wulff, B.C.; Wilgus, T.A. Mast cell activity in the healing wound: More than meets the eye? *Exp. Dermatol.* **2013**, *22*, 507–510. [CrossRef] [PubMed]

3. Mohammadnejad, J.; Yazdian, F.; Omid, M.; Rostami, A.D.; Rasekh, B.; Fathinia, A. Graphene oxide/silver nanohybrid: Optimization, antibacterial activity and its impregnation on bacterial cellulose as a potential wound dressing based on GO-Ag nanocomposite-coated BC. *Eng. Life Sci.* **2018**, *18*, 298–307. [CrossRef] [PubMed]
4. Cheng, G.; Li, B. Nanoparticle-based photodynamic therapy: New trends in wound healing applications. *Mater. Today Adv.* **2020**, *6*, 100049. [CrossRef]
5. Khan, S.; Ul-Islam, M.; Khattak, W.A.; Ullah, M.W.; Park, J.K. Bacterial cellulose-titanium dioxide nanocomposites: Nanostructural characteristics, antibacterial mechanism, and biocompatibility. *Cellulose* **2015**, *22*, 565–579. [CrossRef]
6. Gutiérrez, D.J.R.; Mathews, N.R.; Martínez, S.S. Photocatalytic activity enhancement of TiO<sub>2</sub> thin films with silver doping under visible light. *J. Photochem. Photobiol. A Chem.* **2013**, *262*, 57–63. [CrossRef]
7. Harikishore, M.; Sandhyarani, M.; Venkateswarlu, K.; Nellaippan, T.; Rameshbabu, N. Effect of Ag doping on antibacterial and photocatalytic activity of nanocrystalline TiO<sub>2</sub>. *Procedia Mater. Sci.* **2014**, *6*, 557–566. [CrossRef]
8. Akhavan, O.; Abdollahad, M.; Abdi, Y.; Mohajerzadeh, S. Synthesis of titania/carbon nanotube heterojunction arrays for photoinactivation of E. coli in visible light irradiation. *Carbon* **2009**, *47*, 3280–3287. [CrossRef]
9. Shahmoradi, S.; Golzar, H.; Hashemi, M.; Mansouri, V.; Omid, M.; Yazdian, F.; Yadegari, A.; Tayebi, L. Optimizing the nanostructure of graphene oxide/silver/arginine for effective wound healing. *Nanotechnology* **2018**, *29*, 475101. [CrossRef]
10. Behboudi, H.; Mehdipour, G.; Safari, N.; Pourmadadi, M.; Saei, A.; Omid, M.; Tayebi, L.; Rahmandoust, M. Carbon Quantum Dots in Nanobiotechnology. In *Nanomaterials for Advanced Biological Applications*; Springer: Berlin/Heidelberg, Germany, 2019; pp. 145–179.
11. Gao, M.X.; Liu, C.F.; Wu, Z.L.; Zeng, Q.L.; Yang, X.X.; Wu, W.B.; Li, Y.F.; Huang, C.Z. A surfactant-assisted redox hydrothermal route to prepare highly photoluminescent carbon quantum dots with aggregation-induced emission enhancement properties. *Chem. Commun.* **2013**, *49*, 8015–8017. [CrossRef]
12. Rahmandoust, M.; Ayatollahi, M.R. *Nanomaterials for Advanced Biological Applications*; Springer: Berlin/Heidelberg, Germany, 2019; Volume 104.
13. Tao, H.; Yang, K.; Ma, Z.; Wan, J.; Zhang, Y.; Kang, Z.; Liu, Z. In vivo NIR fluorescence imaging, biodistribution, and toxicology of photoluminescent carbon dots produced from carbon nanotubes and graphite. *Small* **2012**, *8*, 281–290. [CrossRef]
14. Malmir, S.; Karbalaee, A.; Pourmadadi, M.; Hamed, J.; Yazdian, F.; Navaee, M. Antibacterial properties of a bacterial cellulose CQD-TiO<sub>2</sub> nanocomposite. *Carbohydr. Polym.* **2020**, *234*, 115835. [CrossRef]
15. Hashemi, M.; Yadegari, A.; Yazdanpanah, G.; Omid, M.; Jabbehdari, S.; Haghirsadat, F.; Yazdian, F.; Tayebi, L. Normalization of doxorubicin release from graphene oxide: New approach for optimization of effective parameters on drug loading. *Biotechnol. Appl. Biochem.* **2017**, *64*, 433–442. [CrossRef]
16. Rehman, S.R.U.; Augustine, R.; Zahid, A.A.; Ahmed, R.; Tariq, M.; Hasan, A. Reduced Graphene Oxide Incorporated GelMA Hydrogel Promotes Angiogenesis For Wound Healing Applications. *Int. J. Nanomed.* **2019**, *14*, 9603–9617. [CrossRef]
17. Smith, A.T.; LaChance, A.M.; Zeng, S.; Liu, B.; Sun, L. Synthesis, properties, and applications of graphene oxide/reduced graphene oxide and their nanocomposites. *Nano Mater. Sci.* **2019**, *1*, 31–47. [CrossRef]
18. Mukherjee, S.; Sriram, P.; Barui, A.K.; Nethi, S.K.; Veeriah, V.; Chatterjee, S.; Suresh, K.I.; Patra, C.R. Graphene oxides show angiogenic properties. *Adv. Healthc. Mater.* **2015**, *4*, 1722–1732. [CrossRef]
19. Ushio-Fukai, M.; Alexander, R.W. Reactive oxygen species as mediators of angiogenesis signaling. Role of NAD(P)H oxidase. *Mol. Cell. Biochem.* **2004**, *264*, 85–97. [CrossRef]
20. Liu, J.; Yu, Q.; Yu, M.; Li, S.; Zhao, K.; Xue, B.; Zu, H. Silane modification of titanium dioxide-decorated graphene oxide nanocomposite for enhancing anticorrosion performance of epoxy coatings on AA-2024. *J. Alloy. Compd.* **2018**, *744*, 728–739. [CrossRef]
21. Koosha, M.; Mirzadeh, H. Electrospinning, mechanical properties, and cell behavior study of chitosan/PVA nanofibers. *J. Biomed. Mater. Res. Part A* **2015**, *103*, 3081–3093. [CrossRef]
22. Dubey, P.; Bhushan, B.; Sachdev, A.; Matai, I.; Uday Kumar, S.; Gopinath, P. Silver-nanoparticle-incorporated composite nanofibers for potential wound-dressing applications. *J. Appl. Polym. Sci.* **2015**, *132*, 42473. [CrossRef]
23. Koosha, M.; Mirzadeh, H.; Shokrgozar, M.A.; Farokhi, M. Nanoclay-reinforced electrospun chitosan/PVA nanocomposite nanofibers for biomedical applications. *RSC Adv.* **2015**, *5*, 10479–10487. [CrossRef]
24. Jatoi, A.W.; Ogasawara, H.; Kim, I.S.; Ni, Q.-Q. Polyvinyl alcohol nanofiber based three phase wound dressings for sustained wound healing applications. *Mater. Lett.* **2019**, *241*, 168–171. [CrossRef]
25. Norouzi, M.A.; Montazer, M.; Harifi, T.; Karimi, P. Flower buds like PVA/ZnO composite nanofibers assembly: Antibacterial, in vivo wound healing, cytotoxicity and histological studies. *Polym. Test.* **2021**, *93*, 106914. [CrossRef]
26. Dubey, P.; Gopinath, P. PEGylated graphene oxide-based nanocomposite-grafted chitosan/polyvinyl alcohol nanofiber as an advanced antibacterial wound dressing. *RSC Adv.* **2016**, *6*, 69103–69116. [CrossRef]
27. Dash, M.; Chiellini, F.; Ottenbrite, R.M.; Chiellini, E. Chitosan—A versatile semi-synthetic polymer in biomedical applications. *Prog. Polym. Sci.* **2011**, *36*, 981–1014. [CrossRef]
28. Abolghasemzade, S.; Pourmadadi, M.; Rashedi, H.; Yazdian, F.; Kianbakht, S.; Navaei-Nigjeh, M. PVA based nanofiber containing CQDs modified with silica NPs and silk fibroin accelerates wound healing in a rat model. *J. Mater. Chem. B* **2021**, *9*, 658–676. [CrossRef]

29. Mahmoodi, N.M.; Oveisi, M.; Taghizadeh, A.; Taghizadeh, M. Synthesis of pearl necklace-like ZIF-8@ chitosan/PVA nanofiber with synergistic effect for recycling aqueous dye removal. *Carbohydr. Polym.* **2020**, *227*, 115364. [CrossRef]
30. Gerami, S.E.; Pourmadadi, M.; Fatoorehchi, H.; Yazdian, F.; Rashedi, H.; Nigieh, M.N. Preparation of pH-sensitive chitosan/polyvinylpyrrolidone/ $\alpha$ -Fe<sub>2</sub>O<sub>3</sub> nanocomposite for drug delivery application: Emphasis on ameliorating restrictions. *Int. J. Biol. Macromolecules* **2021**, *173*, 409–420. [CrossRef]
31. Samadian, S.; Karbalaee, A.; Pourmadadi, M.; Yazdian, F.; Rashedi, H.; Omid, M.; Malmir, S. A novel alginate-gelatin microcapsule to enhance bone differentiation of mesenchymal stem cells. *Int. J. Polym. Mater. Polym. Biomater.* **2021**, *71*, 395–402. [CrossRef]
32. Zavareh, H.S.; Pourmadadi, M.; Moradi, A.; Yazdian, F.; Omid, M. Chitosan/carbon quantum dot/apramer complex as a potential anticancer drug delivery system towards the release of 5-fluorouracil. *Int. J. Biol. Macromol.* **2020**, *165*, 1422–1430. [CrossRef]
33. Pourmadadi, M.; Shayeh, J.S.; Arjmand, S.; Omid, M.; Fatemi, F. An electrochemical sandwich immunosensor of vascular endothelial growth factor based on reduced graphene oxide/gold nanoparticle composites. *Microchem. J.* **2020**, *159*, 105476. [CrossRef]
34. Salmeh, M.A.; Pourmadadi, M.; Yazdian, F.; Rashedi, H. Antibacterial Polymeric Wound Dressing Based On PVA/Graphene Oxide-Nigella Sativa-Arginine. In Proceedings of the 2020 27th National and 5th International Iranian Conference on Biomedical Engineering (ICBME), Tehran, Iran, 26–27 November 2020; pp. 61–66.
35. Pourmadadi, M.; Shayeh, J.S.; Omid, M.; Yazdian, F.; Alebouyeh, M.; Tayebi, L. A glassy carbon electrode modified with reduced graphene oxide and gold nanoparticles for electrochemical aptasensing of lipopolysaccharides from Escherichia coli bacteria. *Microchim. Acta* **2019**, *186*, 787. [CrossRef]
36. Naderian, N.; Pourmadadi, M.; Rashedi, H.; Yazdian, F. Design of a Novel Nanobiosensor for the Diagnosis of Acute Lymphoid Leukemia (ALL) by Measurement of miRNA-128. In Proceedings of the 2020 27th National and 5th International Iranian Conference on Biomedical Engineering (ICBME), Tehran, Iran, 26–27 November 2020; pp. 41–46.
37. Tabar, F.S.; Pourmadadi, M.; Rashedi, H.; Yazdian, F. Design of Electrochemical Nanobiosensor in the Diagnosis of Prostate Specific Antigen (PSA) Using Nanostructures. In Proceedings of the 2020 27th National and 5th International Iranian Conference on Biomedical Engineering (ICBME), Tehran, Iran, 26–27 November 2020; pp. 35–40.
38. Dinani, H.S.; Pourmadadi, M.; Rashedi, H.; Yazdian, F. Fabrication of nanomaterial-based biosensor for measurement of a microRNA involved in cancer. In Proceedings of the 2020 27th National and 5th International Iranian Conference on Biomedical Engineering (ICBME), Tehran, Iran, 26–27 November 2020; pp. 47–54.
39. Mansur, H.S.; Sadahira, C.M.; Souza, A.N.; Mansur, A.A. FTIR spectroscopy characterization of poly (vinyl alcohol) hydrogel with different hydrolysis degree and chemically crosslinked with glutaraldehyde. *Mater. Sci. Eng. C* **2008**, *28*, 539–548. [CrossRef]
40. Adeli, H.; Khorasani, M.T.; Parvazinia, M. Wound dressing based on electrospun PVA/chitosan/starch nanofibrous mats: Fabrication, antibacterial and cytocompatibility evaluation and in vitro healing assay. *Int. J. Biol. Macromol.* **2019**, *122*, 238–254. [CrossRef]
41. Damayanti, N. Preparation of superhydrophobic PET fabric from Al<sub>2</sub>O<sub>3</sub>-SiO<sub>2</sub> hybrid: Geometrical approach to create high contact angle surface from low contact angle materials. *J. Sol-Gel Sci. Technol.* **2010**, *56*, 47–52. [CrossRef]
42. Golzar, H.; Yazdian, F.; Hashemi, M.; Omid, M.; Mohammadrezaei, D.; Rashedi, H.; Farahani, M.; Ghasemi, N.; Tayebi, L. Optimizing the hybrid nanostructure of functionalized reduced graphene oxide/silver for highly efficient cancer nanotherapy. *New J. Chem.* **2018**, *42*, 13157–13168. [CrossRef]
43. Sothornvit, R.; Olsen, C.; McHugh, T.; Krochta, J. Tensile properties of compression-molded whey protein sheets: Determination of molding condition and glycerol-content effects and comparison with solution-cast films. *J. Food Eng.* **2007**, *78*, 855–860. [CrossRef]
44. Kang, E.B.; Choi, C.A.; Mazrad, Z.A.I.; Kim, S.H.; In, I.; Park, S.Y. Determination of Cancer Cell-Based pH-Sensitive Fluorescent Carbon Nanoparticles of Cross-Linked Polydopamine by Fluorescence Sensing of Alkaline Phosphatase Activity on Coated Surfaces and Aqueous Solution. *Anal. Chem.* **2017**, *89*, 13508–13517. [CrossRef]
45. Irfan, M.; Ahmad, T.; Moniruzzaman, M.; Bhattacharjee, S.; Abdullah, B. Size and stability modulation of ionic liquid functionalized gold nanoparticles synthesized using *Elaeis guineensis* (oil palm) kernel extract. *Arab. J. Chem.* **2020**, *13*, 75–85. [CrossRef]
46. Batista, K.A.; Lopes, F.M.; Yamashita, F.; Fernandes, K.F. Lipase entrapment in PVA/Chitosan biodegradable film for reactor coatings. *Mater. Sci. Eng. C* **2013**, *33*, 1696–1701. [CrossRef]
47. Liu, Y.; Wang, S.; Lan, W. Fabrication of antibacterial chitosan-PVA blended film using electrospray technique for food packaging applications. *Int. J. Biol. Macromol.* **2018**, *107*, 848–854. [CrossRef] [PubMed]
48. Ahmed, J.; Luciano, G.; Schizzi, I.; Arfat, Y.A.; Maggiore, S.; Thai, T.L.A. Non-isothermal crystallization behavior, rheological properties and morphology of poly ( $\epsilon$ -caprolactone)/graphene oxide nanosheets composite films. *Thermochim. Acta* **2018**, *659*, 96–104. [CrossRef]
49. Yang, Y.; Wang, Q.; Qiu, W.; Guo, H.; Gao, F. Covalent immobilization of Cu<sub>3</sub>(btc)<sub>2</sub> at chitosan–electroreduced graphene oxide hybrid film and its application for simultaneous detection of dihydroxybenzene isomers. *J. Phys. Chem. C* **2016**, *120*, 9794–9803. [CrossRef]
50. Abdelrazek, E.; Elashmawi, I.; Labeeb, S. Chitosan filler effects on the experimental characterization, spectroscopic investigation and thermal studies of PVA/PVP blend films. *Phys. B Condens. Matter* **2010**, *405*, 2021–2027. [CrossRef]

51. Zhang, Y.; Wang, X.; Cao, M. Confinedly implanted NiFe 2 O 4-rGO: Cluster tailoring and highly tunable electromagnetic properties for selective-frequency microwave absorption. *Nano Res.* **2018**, *11*, 1426–1436. [CrossRef]
52. Li, W.; Song, B.; Zhang, S.; Zhang, F.; Liu, C.; Zhang, N.; Yao, H.; Shi, Y. Using 3-Isocyanatopropyltrimethoxysilane to decorate graphene oxide with nano-titanium dioxide for enhancing the anti-corrosion properties of epoxy coating. *Polymers* **2020**, *12*, 837. [CrossRef]
53. Osman, Z.; Arof, A.K. FTIR studies of chitosan acetate based polymer electrolytes. *Electrochim. Acta* **2003**, *48*, 993–999. [CrossRef]
54. Lawrie, G.; Keen, I.; Drew, B.; Chandler-Temple, A.; Rintoul, L.; Fredericks, P.; Grøndahl, L. Interactions between alginate and chitosan biopolymers characterized using FTIR and XPS. *Biomacromolecules* **2007**, *8*, 2533–2541. [CrossRef]
55. Santos, C.; Silva, C.J.; Büttel, Z.; Guimarães, R.; Pereira, S.B.; Tamagnini, P.; Zille, A. Preparation and characterization of polysaccharides/PVA blend nanofibrous membranes by electrospinning method. *Carbohydr. Polym.* **2014**, *99*, 584–592. [CrossRef]
56. Sanchez-Alvarado, D.I.; Guzmán-Pantoja, J.; Páramo-García, U.; Maciel-Cerda, A.; Martínez-Orozco, R.D.; Vera-Graziano, R. Morphological study of Chitosan/Poly (vinyl alcohol) nanofibers prepared by electrospinning, collected on reticulated vitreous carbon. *Int. J. Mol. Sci.* **2018**, *19*, 1718. [CrossRef]
57. Gonçalves, R.P.; Ferreira, W.H.; Gouvêa, R.F.; Andrade, C.T. Effect of chitosan on the properties of electrospun fibers from mixed poly (vinyl alcohol)/chitosan solutions. *Mater. Res.* **2017**, *20*, 984–993. [CrossRef]
58. Stankovich, S.; Dikin, D.A.; Piner, R.D.; Kohlhaas, K.A.; Kleinhammes, A.; Jia, Y.; Wu, Y.; Nguyen, S.T.; Ruoff, R.S. Synthesis of graphene-based nanosheets via chemical reduction of exfoliated graphite oxide. *Carbon* **2007**, *45*, 1558–1565. [CrossRef]
59. Štengl, V.; Bakardjieva, S.; Grygar, T.M.; Bludská, J.; Kormunda, M. TiO 2-graphene oxide nanocomposite as advanced photocatalytic materials. *Chem. Cent. J.* **2013**, *7*, 41. [CrossRef]
60. Jung, H.-G.; Myung, S.-T.; Yoon, C.S.; Son, S.-B.; Oh, K.H.; Amine, K.; Scrosati, B.; Sun, Y.-K. Microscale spherical carbon-coated Li 4 Ti 5 O 12 as ultra high power anode material for lithium batteries. *Energy Environ. Sci.* **2011**, *4*, 1345–1351. [CrossRef]
61. Debrah, P.; Kwapong, A.A.; Fredua-Agyeman, M. Treatment of Biofilms in Infected Wounds. In *Therapeutic Dressings and Wound Healing Applications*; John Wiley & Sons: Hoboken, NJ, USA, 2020; pp. 115–136.
62. Li, H.; Shi, W.; Zeng, X.; Huang, S.; Zhang, H.; Qin, X. Improved desalination properties of hydrophobic GO-incorporated PVDF electrospun nanofibrous composites for vacuum membrane distillation. *Sep. Purif. Technol.* **2020**, *230*, 115889. [CrossRef]
63. Li, H.; Shi, W.; Zhang, H.; Zhou, R.; Qin, X. Preparation of internally pressurized polyamide thin-film composite hollow fiber nanofiltration membrane with high ions selectivity by a facile coating method. *Prog. Org. Coat.* **2019**, *139*, 105456. [CrossRef]
64. Zahirifar, J.; Karimi-Sabet, J.; Moosavian, S.M.A.; Hadi, A.; Khadiv-Parsi, P. Fabrication of a novel octadecylamine functionalized graphene oxide/PVDF dual-layer flat sheet membrane for desalination via air gap membrane distillation. *Desalination* **2018**, *428*, 227–239. [CrossRef]
65. Agrawal, P.; Pramanik, K. Chitosan-poly (vinyl alcohol) nanofibers by free surface electrospinning for tissue engineering applications. *Tissue Eng. Regen. Med.* **2016**, *13*, 485–497. [CrossRef]
66. Alhosseini, S.N.; Moztarzadeh, F.; Mozafari, M.; Asgari, S.; Dodel, M.; Samadikuchaksaraei, A.; Kargozar, S.; Jalali, N. Synthesis and characterization of electrospun polyvinyl alcohol nanofibrous scaffolds modified by blending with chitosan for neural tissue engineering. *Int. J. Nanomed.* **2012**, *7*, 25.
67. Zahouani, H.; Pailler-Mattei, C.; Sohm, B.; Vargiolu, R.; Cenizo, V.; Debret, R. Characterization of the mechanical properties of a dermal equivalent compared with human skin in vivo by indentation and static friction tests. *Ski. Res. Technol.* **2009**, *15*, 68–76. [CrossRef]
68. Tobin, D.J. Introduction to skin aging. *J. Tissue Viability* **2017**, *26*, 37–46. [CrossRef] [PubMed]
69. Bagher, Z.; Ehterami, A.; Safdel, M.H.; Khastar, H.; Semiari, H.; Asefnejad, A.; Davachi, S.M.; Mirzaii, M.; Salehi, M. Wound healing with alginate/chitosan hydrogel containing hesperidin in rat model. *J. Drug Deliv. Sci. Technol.* **2020**, *55*, 101379. [CrossRef]
70. Alavarse, A.C.; de Oliveira Silva, F.W.; Colque, J.T.; da Silva, V.M.; Prieto, T.; Venancio, E.C.; Bonvent, J.-J. Tetracycline hydrochloride-loaded electrospun nanofibers mats based on PVA and chitosan for wound dressing. *Mater. Sci. Eng. C* **2017**, *77*, 271–281. [CrossRef] [PubMed]
71. Abdelgawad, A.M.; Hudson, S.M.; Rojas, O.J. Antimicrobial wound dressing nanofiber mats from multicomponent (chitosan/silver-NPs/polyvinyl alcohol) systems. *Carbohydr. Polym.* **2014**, *100*, 166–178. [CrossRef] [PubMed]
72. Zhou, L.; Yu, K.; Lu, F.; Lan, G.; Dai, F.; Shang, S.; Hu, E. Minimizing antibiotic dosage through in situ formation of gold nanoparticles across antibacterial wound dressings: A facile approach using silk fabric as the base substrate. *J. Clean. Prod.* **2020**, *243*, 118604. [CrossRef]
73. Motawea, A.; Abd El-Gawad, A.E.-G.H.; Borg, T.; Motawea, M.; Tarshoby, M. The impact of topical phenytoin loaded nanostructured lipid carriers in diabetic foot ulceration. *Foot* **2019**, *40*, 14–21. [CrossRef]
74. Motealleh, B.; Zahedi, P.; Rezaeian, I.; Moghimi, M.; Abdolghaffari, A.H.; Zarandi, M.A. Morphology, drug release, antibacterial, cell proliferation, and histology studies of chamomile-loaded wound dressing mats based on electrospun nanofibrous poly ( $\epsilon$ -caprolactone)/polystyrene blends. *J. Biomed. Mater. Res. Part B Appl. Biomater.* **2014**, *102*, 977–987. [CrossRef]
75. Marulasiddeshwara, R.; Jyothi, M.; Soontarapa, K.; Keri, R.S.; Velmurugan, R. Nonwoven fabric supported, chitosan membrane anchored with curcumin/TiO<sub>2</sub> complex: Scaffolds for MRSA infected wound skin reconstruction. *Int. J. Biol. Macromol.* **2020**, *144*, 85–93. [CrossRef]

76. Bolle, E.C.; Bartnikowski, N.; Haridas, P.; Parker, T.J.; Fraser, J.F.; Gregory, S.D.; Dargaville, T.R. Improving skin integration around long-term percutaneous devices using fibrous scaffolds in a reconstructed human skin equivalent model. *J. Biomed. Mater. Res. Part B Appl. Biomater.* **2020**, *108*, 738–749. [CrossRef]
77. Murphy, S.V.; Skardal, A.; Nelson, R.A., Jr.; Sunnon, K.; Reid, T.; Clouse, C.; Kock, N.D.; Jackson, J.; Soker, S.; Atala, A. Amnion membrane hydrogel and amnion membrane powder accelerate wound healing in a full thickness porcine skin wound model. *Stem Cells Transl. Med.* **2020**, *9*, 80–92. [CrossRef]